Juho Hautala

Light-Induced Motions in Azopolymer Films Doped with Silver Nanoparticles

School of Science

Thesis submitted for examination for the degree of Master of Science in Technology.

Espoo, January 29, 2014

Thesis supervisor:

Prof. Matti Kaivola

Thesis instructor:

D.Sc. (Tech.) Jaana Vapaavuori

Aalto University
School of Science

AALTO UNIVERSITY
SCHOOL OF SCIENCE

ABSTRACT OF THE
MASTER'S THESIS

Author: Juho Hautala

Title: Light-Induced Motions in Azopolymer Films Doped with Silver Nanoparticles

Date: January 29, 2014 Language: English Number of pages:8+49

Department of Applied Physics

Professorship: Optics Code: F3004

Supervisor: Prof. Matti Kaivola

Instructor: D.Sc. (Tech.) Jaana Vapaavuori

In this thesis, the light-induced phenomena in azobenzene-containing polymer films are studied. Light-induced phenomena, such as formation of surface-relief gratings and light-induced birefringence, are typical for azobenzene-containing materials and enable a wide range of applications ranging from optical components to telecommunication technology, and beyond. The objective is to enhance these phenomena via local field enhancement of the incident field by adding silver nanoparticles into the azopolymer films.

Mie efficiencies for spherical nanoparticles in the used azobenzene-polymer medium are calculated for different sizes. Also the experimental setups for inscription of surface-relief gratings and photo-induced birefingence are presented, along with a setup for measuring the lifetime of *cis* isomer of an azobenzene molecule. The experiments are performed for azobenzene-containing films doped with 8, 30 and 50 nanometer silver nanoparticles, with silver/azopolymer mass ratios ranging from 0 to 2%. With 8 nanometer particles, also mass ratios up to 10% are studied.

In general, the results indicate a significant decrease in the surface-relief grating formation and photo-induced birefringence with increased nanoparticle concentration. However, a modest increase in the studied phenomena on certain amounts of silver nanoparticles is achieved. It can also be concluded that also other factors than the local field enhancement affect the light-induced processes, such as light scattering or damping mechanisms of nanoparticles with a diameter of several tens of nanometers. In the future studies it is recommended to use particles smaller than 30 nanometers in diameter. For the surface plasmon resonance and the absorption of azopolymer to overlap, also a change of the nanoparticle material is recommended.

Keywords: optics, light-induced, nanoparticles, azobenzene, surface plasmon

AALTO-YLIOPISTO
PERUSTIETEIDEN KORKEAKOULU

DIPLOMITYÖN
TIIVISTELMÄ

Tekijä: Juho Hautala

Työn nimi: Valoherätteiset liikkeet hopeananohiukaksia sisältävissä atsopolymeerikalvoissa

Päivämäärä: January 29, 2014 Kieli: Englanti Sivumäärä:8+49

Teknillisen fysiikan laitos

Professuuri: Optiikka Koodi: F3004

Valvoja: Prof. Matti Kaivola

Ohjaaja: TkT Jaana Vapaavuori

Tässä työssä tutkitaan valoherätteisiä ilmiöitä atsobentseenejä sisältävissä ohutkalvoissa. Valoherätteiset ilmiöt, kuten valoherätteinen pintahilamuodostus ja valoherätteinen kahtaistaittavuus, ovat tyypillisiä atsobentseenejä sisältäville materiaaleille ja ne tarjoavat uusia mahdollisuuksia esimerkiksi optisten komponenttien ja telekommunikaatioteknologian kehityksessä. Työn tavoite on vahvistaa näitä ilmiöitä paikallisen lähikenttävahvistuksen avulla lisäämällä hopeananohiukkasia atsobentseenejä sisältäviin polymeerikalvoihin.

Mie-tehokkuudet lasketaan erikokoisille hopeananohiukkasille käytetyssä väliaineessa. Myös käytännön koejärjestelyt valoherätteisen pintahilan ja valoherätteisen kahtaistaittavuuden kirjoittamista varten, sekä koejärjestely atsobentseenin *cis*-isomeerin elinajan mittaamiseksi esitellään. Kokeet suoritetaan atsobentseenejä sisältävillä kalvoilla, joihin on lisätty halkaisijaltaan 8, 30 ja 50 nanometrin hopeahiukkasia. Hopean ja polymeeriväliaineen massojen suhde vaihtelee välillä 0-2%. 8 nanometrin hiukkasia tutkittiin 10%:iin asti.

Yleisesti tulokset osoittavat pintahilamuodostuksen ja valoherätteisen kahtaistaittavuuden merkittävää heikentymistä nanohiukkaspitoisuuden kasvaessa. Kuitenkin tietyillä hopeananohiukkaspitoisuuksilla tutkitut ilmiöt voimistuvat hieman. Tuloksista voidaan myös päätellä, että tutkituilla näytteillä paikalliskentän vahvistuminen ei ole ainoa valoherätteisiin ilmiöihin vaikuttava tekijä, vaan imiöihin vaikuttavat esimerkiksi valon sironta ja plasmoniresonanssin vaimennusmekanismit etenkin suuremmilla nanohiukkasilla. Jatkotutkimuksia ajatellen on suositeltavaa käyttää nanohiukkasia, joiden halkaisija on pienempi kuin 30 nanometriä. Jotta nanohiukkasten plasmoniresonanssi ja atsobentseenin absorbanssi osuisivat samoille aallonpituuksille, myös nanohiukkasten materiaalin vaihto on suositeltavaa.

Avainsanat: optiikka, valoherätteinen, nanohiukkaset, atsobentseeni, pintaplasmoni

Preface

During the process of preparing this thesis, I have received creditable support from various people. First of all, I would like to thank my supervisor Prof. Matti Kaivola for the opportunity to be part of the Optics group, and my instructor Jaana Vapaavuori, who has been a great inspiration since the beginning. I would also like to thank Arri and Robert for the scientific support, fellow workers Aleksi and Ismo, and of course the home front Minna. Thanks and apologies.

Otaniemi, January 29, 2014

Juho Hautala

Contents

Symbols and Abbreviations

Symbols

A	Absorbance
A_i	Amplitudes for biexponential fitting equation
a_n, b_n	Scattering coefficients for Helmholz equation
α	Absorption coefficient
α_p	Complex polarizability
c	Speed of light in vacuum
C_{abs}, C_{scat}	Effective cross-sections for absorption and scattering
d	Estimated interparticle distance
ϵ_r	Relative permittivity
ϵ_{trans}, ϵ_{cis}	Extinction coefficients for *trans* and *cis* isomers
η	1st order diffraction efficiency
γ	Thermal relaxation constant
h	Film thickness
I	Measured signal
I_0	Reference signal
k	Wave-number
k_t	Time constant from *cis* lifetime fit
K	Imaginary part of refractive index
λ	Wavelength
Λ	Grating period
n	Non-bonding molecular orbital; summation index; refractive index
Δn	Birefringence
n_o	Refractive index along the ordinary optical axis
n_e	Refractive index along the extraordinary optical axis
ω	Angular frequency of light
Φ_{trans}, Φ_{cis}	Quantum yields of photoisomerization for *trans* and *cis* isomers
ϕ	Angle between the light polarization and the azo dipole axis
π	Bonding molecular p-orbital; π
π^*	Antibonding molecular p-orbital
Q_i	Mie efficiency for absorption, scattering or extinction (i = abs, sca, ext)
r	Radial distance from a point
R	Particle radius
t	Time
τ_i	Time constant for biexponential fitting
T_g	Glass transition temperature
θ	Incident angle

Abbreviations

AFM	Atomic force microscopy
Ag	Silver
AgNP	Silver nanoparticle
BF	Birefringence
DR1	Disperse Red 1
DY7	Disperse Yellow 7
LCP	Left-handed circular (polarization)
NP	Nanoparticle
p4VP	Poly(4-vinylpyridine)
pDR1a	poly(Disperse Red 1)acrylate (poly[4'-[((2-(acryloyloxy)ethyl)ethyl)amino]-4-nitroazobenzene)
p-p	SRG inscription geometry with two interfering p-polarized waves (E-field components in the grating vector direction)
PQE	Photo-isomerization quantum efficiency
PVP	Poly(vinylpyrrolidone)
RCP-LCP	SRG inscription geometry with interfering right- and left-handed circularly polarized waves
UV	Ultraviolet
RCP	Right-handed circular (polarization)
s-s	SRG inscription geometry with two interfering s-polarized waves (no E-field component in the grating vector direction)
SEM	Scanning electron microscopy
SPN	Surface plasmons on metal nanoparticles
SPR	Surface plasmon resonance
SRG	Surface-relief grating

1 Introduction

Even if the term optics was introduced in 1704, it can be stated that optics is one of the oldest forms of natural sciences, having its origins in astronomy and geometry [1, 2]. The development still goes on, as optics plays a major role in modern communication technology and also in many analytical applications, to name a few [3]. A popular example of the intriguing history of optics is the Lycurgus Cup from the 4th century AD [4]. In this item, metallic nanoparticles were exploited in order to create what we today know to be dichroic glass. It took scientists over a millennium and a half to fully understand, what is the secret behind this enchanting item. New frontiers in optics are constantly being discovered also in other fields of science, for example in materials science.

Materials science is required to construct a basis for modern, sustainable technology, and using optical materials is a noteworthy tool in achieving sustainable, efficient and elegant solutions to meet the constantly growing demand. The strong connection between optics and materials science is obvious when studying light-responsive materials [3]. Such materials exist all around us, for instance in the human eye [5].

A few decades back, researchers found out about the light-responsive properties of the widely used commercial dyes, azobenzenes [6]. Since then, the interesting light-induced phenomena in these materials have been under the loop of scientists. The responsiveness of azobenzene-containing polymers to light is now known to be due to photon-triggered isomerization between the two isomers of azobenzene molecules. Even though the light-induced phenomena have been studied for a few decades already, the fundamental mechanisms behind some of the phenomena triggered by the isomerization process still remain a mystery [7]. Plasmonics and nanostructures have also attained more and more interest in recent years, as technology urgently seeks for solutions to encapsulate more information and processing capacity on smaller spatial units.

This thesis combines both materials science and optics in order to enhance the light-induced phenomena of azobenzene-containing polymer films with local field enhancement by metallic nanoparticles. Surface-plasmon resonances on metallic nanoparticles are today harnessed for several applications on different fields of study [8]. However, there are only few studies on how the surface-plasmon resonances affect the light-induced isomerization of azobenzene molecules and the phenomena it gives rise to.

In order to study these phenomena, thin films of azobenzene-containing polymers are studied with different methods. Silver nanoparticles of different sizes are incorporated into the polymer matrix to produce a random distribution of nanoparticles, which have a surface-plasmon resonance frequency near the absorption maximum of the thin film. The nanoparticles are expected to affect the isomerization rate of the azobenzene molecules, which could affect the dynamics of the light-induced phenomena.

In this thesis it is concluded that the number of factors that should be accounted for while performing such experiments is larger than expected. The results show an

unexpected decrease in the efficiency of the light-induced phenomena studied. This is most likely due to aggregation and oxidation of the nanoparticles in the films. Additionally, even if the size of the exploited nanoparticles leads to the surface plasmon resonance frequency to lie near the exposure wavelengths, the damping mechanisms begin to play a significant role in the performance of the system.

This thesis is organized as follows. The properties of azobenzenes and basics of plasmonics are introduced in Sec. 2. A method to calculate the Mie efficiencies in an absorbing medium for theoretical backup of the thesis is presented in Sec. 3. The experimental section of the thesis concentrates on the light-induced phenomena of azobenzene-containing materials, such as light-induced birefringence and surface-relief grating formation. The experimental setups to study these phenomena are presented in Sec. 4.2. In addition, the basics of the two nanomicroscopic imaging techniques used in this work are presented. The results of the experimental studies are presented in Sec. 5, and Sec. 6 includes the conclusions of this thesis.

2 Background

The properties of azobenzene derivatives have been studied for applications such as dyes, molecular probes, electro-optic liquid crystals, and materials for nonlinear optics and optical storage for over three decades now [7]. Even though the light responsiveness of azobenzene was firstly reported in 1934 [9], it began to gain interest in the field of optics in the 1980s as photo-induced birefringence gratings were firstly reported [6]. Photo-induced macroscopic motion in an azobenzene containing polymer thin film was reported in 1995 [7, 10, 11]. That brought forth the light-induced isomerization of azobenzene to be one of the topics of interest in materials science [7]. This section consists of a review of the properties of azobenzene molecules, especially the photoisomerization and the resulting phenomena: photo-orientation and surface mass transport. Also, a short introduction to plasmonics and Mie theory, and in the end, a couple of studies on the interaction between plasmons and azobenzenes are presented.

2.1 Azobenzene Properties

Azobenzene is a molecule, where two phenyl rings are separated by a nitrogen double bond, an azo-bond (-N=N-). The name azo comes from the French name for nitrogen, *azote*. In the last century, azobenzenes have been used as commercial dyes because of their intensive color due to their extensive conjugated π-electron system and wide spectral range of absorption that can be tailored within the visible region of light [7].

Azobenzenes can be divided into three categories: azobenzene-type molecules, aminoazobenzene-type molecules, and pseudostilbene-type molecules [7, 12]. This classification is based on the energetic ordering of their (n,π^*) and (π, π^*) states. These states affect the energy transfers in the electron transitions during the isomerization process, and thus also the spectral properties (explained in Sec. 2.1.1). The classification can also be done purely based on the spectral properties of the compound, which has roughly the same outcome as the energy state classification. In this thesis, azobenzene refers to azobenzene molecules and their derivatives. [3, 12]

2.1.1 Photoisomerization

Photoisomerization means that a molecule can change its geometry upon photon absorption. Azobenzenes have two isomers, a *trans* form that is a rodlike molecule and a *cis* form, where the phenyl rings of the molecule are twisted at ca. 90° relative to the C-N=N-C plane [13]. The isomers of an azobenzene molecule are illustrated in Fig. 1(a).

In most cases, azobenzene is a term used to describe a group of azobenzene derivatives, which are azobenzene molecules with different substituents, typically at the 4, 4' positions. By modifying these substituents, the azobenzene can be tailored to be responsive in various wavelengths ranging from ultraviolet (UV) to red in the visible region of the spectrum. The tailoring of azobenzene derivatives is based

on the π-electron delocalisation of the structure that changes depending on the substituents. Azobenzene-type molecules are similar to unsubstituted azobenzenes. Their transition from a bonding p-orbital to an antibonding p-orbital ($\pi \rightarrow \pi^*$ transition) that is mostly accounting for the *trans* $\rightarrow$ *cis* isomerization lies in the UV region, and the transition from a non-bonding orbital to antibonding p-orbital (n $\rightarrow$ π^* transition) that is mostly accounting for the *cis* $\rightarrow$ *trans* isomerization lies in the visible region of the spectrum. When azobenzene is substituted with an electron-donating amino group (-NH_2) to yield an aminoazobenzene-type molecule, the $\pi \rightarrow \pi^*$ transition band is moved closer to the n $\rightarrow$ π^* band in the visible region of light. The pseudostilbene-types have both acceptor and donor substitutions, which leads to overlapping of the absorption spectra of *trans* and *cis* states at blue-green wavelengths. [3]

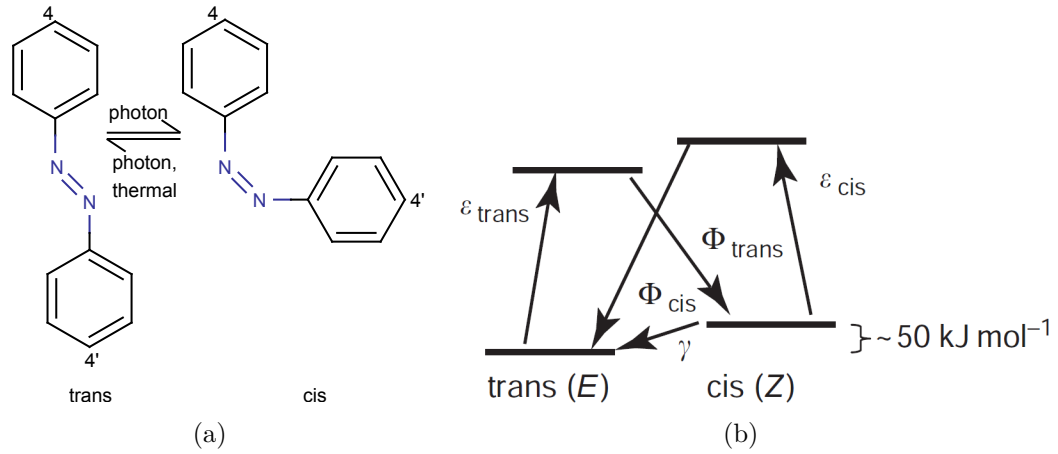

Figure 1: (a) Azobenzene can transform between *trans* and *cis* states photochemically and relax to the more stable *trans* state thermally. (b) Simplified state model for plain azobenzene. The *trans* and *cis* extinction coefficients are denoted by ϵ_{trans} and ϵ_{cis}. Symbol Φ refers to the quantum yields of photoisomerization, and γ is the thermal relaxation rate constant [3].

Photon-triggered isomerization, also known as photo-isomerization, is typical for azobenzenes and their derivatives. The photo-isomerization is a highly efficient and chemically completely reversible process between the two states: the thermally stable *trans* form and the metastable *cis* form. The metastability of the *cis* isomer refers to its ability to transform back to the *trans* state thermally. The isomerization from *trans* to *cis* state causes the distance between the 4 and 4' positions to reduce from ca. 1.0 nm to ca. 0.6 nm. However, the free-volume requirement of the molecule will increase. Also the dipole moment of the molecule increases from zero to 3.1 D for an unsubstituted azobenzene [3]. The exact three-dimensional geometries of the isomers also depend on the π-electron delocalisation, as the atom bonding angles are defined by the molecular energy states [13]. The structures illustrated in Fig. 1(a) are therefore simplifications in the C-N=N-C plane.

The energies of transition states of a plain azobenzene molecule are illustrated in Fig. 1(b). The isomerizations are free from side reactions and occur in time scales of

picoseconds. As the absorption wavelength of the azobenzene molecule, also the time scale for the thermal relaxation, or backisomerization to the *trans* state depends on the electron delocalization. The time scale of the thermal backisomerization can range between milliseconds and hours, in a proper environment even years. The backisomerization can also be triggered by a photon that corresponds to the azobenzene molecule's *cis* absorption band. [3]

An azobenzene-containing system can reach a photostationary state during irradiation either in a solution, or in a bulky sample, where azobenzene chromophores are in a polymer matrix. A photostationary state is a state, where the ratio of chromophores in *cis* and *trans* states is constant. The steady-state composition is unique to each system, and is dependent on the quantum yields for the two isomerization processes and the thermal relaxation. As the ring substitution affects both the absorption spectrum of the *trans* and *cis* states, the irradiating light can enhance both quantum yields, leading to rapid cycling between the isomerization states. The cycling plays a significant role in the photo-induced mass transport that is discussed in more detail in Sec. 2.1.3. [3]

2.1.2 Photo-alignment and Birefringence

For the molecules to be excited and the photo-isomerization to occur, the incident light has to have a polarization component parallel to the chromophore's transition dipole moment [11]. For rod-like molecules such as azobenzenes, the excitation probability will vary as $\cos^2\phi$, where ϕ is the angle between the light polarization and the azo dipole axis [3]. By thermal relaxation, the chromophore isomerizes to

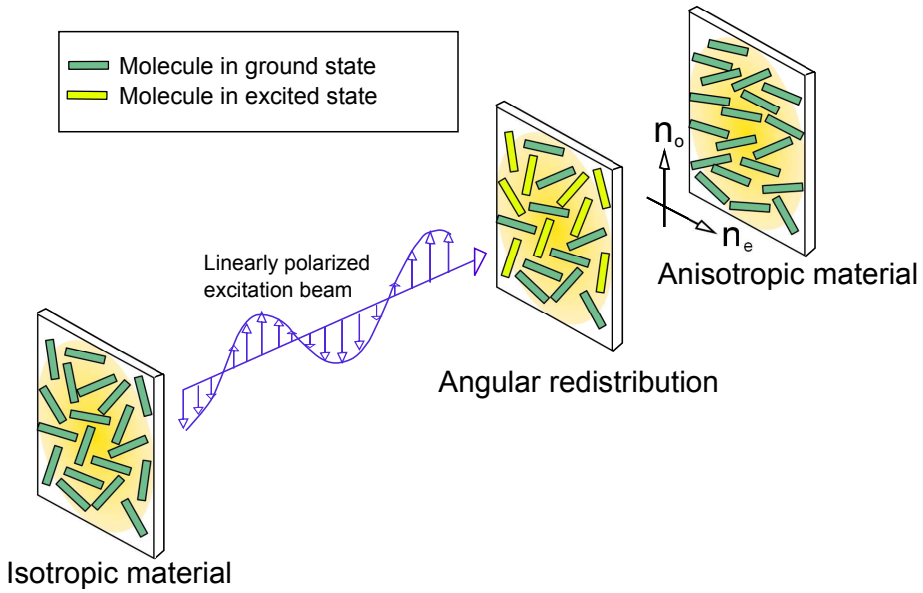

Figure 2: Schematic of photo-alignment under excitation with linearly polarized light. The molecules that have dipole moment parallel to the polarization of the excitation beam are excited and finally relax to an alignment where the dipole moment is perpendicular to the polarization of the excitation beam [12].

a random alignment. In an ideal case, as the irradiation with linearly polarized light is continuous for a long enough time, the bulk containing these chromophores reaches a state, where the majority of the chromophores have reached an alignment containing no component of transition dipole moment parallel to the incident beam polarization. That is, the chromophores become aligned either in the direction along the incident irradiation beam, or in the plane of the film perpendicular with respect to the polarization of the irradiation beam. In reality, a typical order parameter for an amorphous azobenzene-containing sample rarely exceeds 0.1 [12]. The molecular orientation under linearly polarized light is illustrated in Fig. 2. Isotropy can be restored either by unpolarized or circularly polarized incident light, apart from the orientation along the incident beam. [3, 11]

As a result of this statistical reorientation, photo-induced birefringence and dichroism can be induced into an azo-containing system. Birefringence means anisotropy in the refractive index of the material for the ordinary and extraordinary waves, and is defined as $\Delta n = n_o - n_e$, where n_o and n_e are the refractive indices along the ordinary and extraordinary waves, respectively. Dichroism means that the absorption coefficient of the material is anisotropic with respect to the polarization of the incident light. The direction of the orientation can be controlled by the polarization of the incident beam. By manipulation of the incident beam, it is possible to create diffractive gratings based on a local change in the birefringence of the material. Azobenzene-containing systems have been reported to achieve birefringence values of up to 0.5 [14]. The first birefringence grating on an azobenzene-containing, amorphous polymer was reported by Todorov *et al.* in 1984 [6]. The diffractive properties of azopolymer diffraction gratings were then assumed to be due to the birefringence only, until a formation of surface relief grating was reported [10]. The erasability of the birefringence makes azo-containing materials a promising option for being used as tunable waveplates, all-optical switches in optical computing, or in holographic applications. [3]

2.1.3 Mass Transport

In 1995, over ten years after the discovery of the reversible birefringence gratings, a large-scale surface mass transport in azobenzene-containing polymer films was reported [10]. It was observed that as the films were irradiated by a light interference pattern, the surface of the sample was deformed according to the interference pattern. The sample used in the experiments by Rochon *et al.* was a thin spin-cast polymer film from poly Disperse Red 1 acrylate (pDR1a), a pseudostilbene side-chain azopolymer [10]. The phenomenon occurs well below the glass transition temperature (T_g) of the amorphous material, and allows formation of surface-relief grating structures (SRG) with modulation depths in a range of several hundreds of nanometers and grating periodicities larger than the irradiation wavelength. The intensity of the irradiation laser can be well below that required for ablation, and the heating effect at a typical inscription intensity is negligible [12]. The surface mass transport is also highly dependent on the polarization of the incident beam. It has

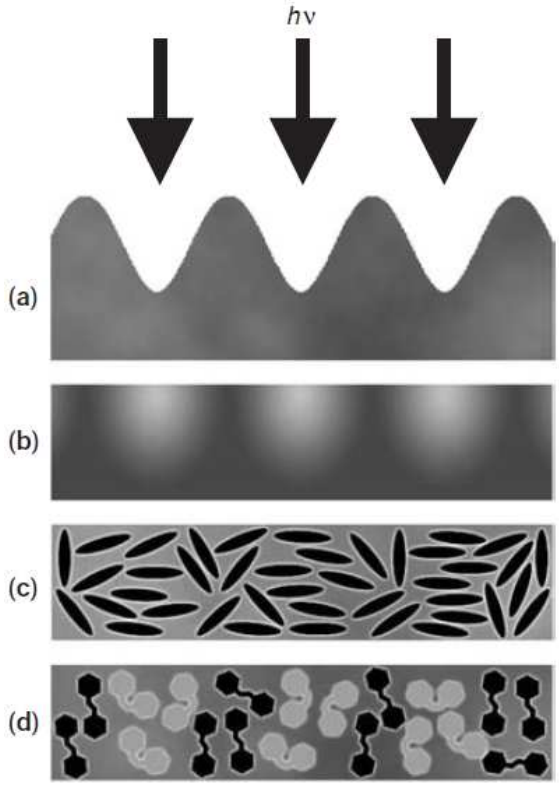

Figure 3: Schematic of the different gratings that are formed during illumination of an azo sample. (a) Surface-relief Grating (b) Density Grating (c) Orientational Grating (birefringence) (d) Photochemical Grating (photostationary state). [3]

been shown that inscription with interference patterns created with p-p[1] and RCP-LCP[2] geometries give rise to much stronger surface-relief gratings than those created with s-s[3] geometry due to a polarization gradient along the grating vector. [3, 15, 16]

The surface mass transport effect still lacks an explanation that would cover all the aspects that have been observed experimentally, but there are several theories about it. Among the first theories, there was a model derived from basic Newtonian dynamic relations of viscous fluids in 1998 [16]. The model is mostly based on the free volume requirement of the chromophores, and therefore it does not account for some observations of the polarization dependence and correlates with the experimental data only on low modulation depths. The model was refined later by Sumaru *et al.* to cover the whole range of modulation depths by including the interference wave number [17]. A photo-induced diffusion model was introduced by Lefin *et al.* also in 1998. The model assumes that the concentration is directly proportional to the grating height [18].

The early models that were based on pressure gradients and thermal effects can not describe the cases, where the inscription intensity is spatially constant and only

[1]two interfering p-polarized waves (E-field components in the grating vector direction)
[2]interfering right- and left-handed circularly polarized waves
[3]two interfering s-polarized waves (no E-field component in the grating vector direction)

the polarization state of the total field varies. A completely different approach based on an optical gradient force was presented by Kumar *et al.*, also in 1998 [19]. This model is capable of explaining the strong polarization dependency of the process, as it shows a correlation between the force density due to the optically induced polarization and the derivative of the incident intensity pattern. Another model that takes the polarization state into account, by Pedersen *et al.*, is based on a slightly modified version of the mean-field theory [20]. However, the calculated forces that drive the mass transport according to these calculations are two orders of magnitude smaller than the force effect of the gravitational field [21].

A new thermodynamic approach was introduced by Saphiannikova *et al.* in 2005, which takes into account the azobenzene chromophore reorientation and the induction of plastic deformation during the irradiation [21]. Other more recent suggestions include a statistical model by Juan *et al.* [22], and a molecular model by Ambrosio *et al.* [23] that are both based on the diffusion model.

The only thing in common with the different models is that they all require cycling of *trans-cis-trans* isomerizations. Even if the fundamental driving mechanism remains unsolved, it is quite safe to state that the mass transport effect arises from a combination of several factors. Whilst exposure of the azobenzene-containing materials gives rise to several phenomena, it is no surprise that also different kinds of gratings are formed. The different gratings are illustrated in Fig. 3. Some of the gratings, such as the photochemical grating, persist only during the irradiation. In the cases, where the SRG is overwhelming the other effects, the formation of the other gratings can only be observed in the very beginning of the irradiation when their proportional contribution is at highest. [3]

The simplest way of making surface relief gratings is by using a Lloyd mirror setup, which is explained in more detail in Sec. 4.2.2. The very fundamental idea of the setup is that the sample is exposed to a sinusoidal intensity pattern. The material will migrate from the illuminated regions to the areas, where the electric-field component parallel to the grating vector is absent, or not spatially modulated [15]. An example of an atomic force microscopy (AFM) image of a sinusoidal surface-relief grating is illustrated in Fig. 4. The formation of a surface-relief grating by surface mass transport is one of the key tools to study the materials' optical properties in this thesis.

Figure 4: An example of surface-relief grating topology inscribed on an azobenzene-containing polymer thin film.

2.2 Plasmonics

Nanophotonics is a growing field of research in optics. Earliest examples of employing metallic nanostructures include the famous Lycurgus cup from the Byzantine Empire in the 4th century AD that changes colour whether the light is transmitted through or reflected by the glass. The material in the cup is known to be dichroic glass, and the phenomenon rises from "contamination" from silver dust. The phenomenon was theoretically explained already in the beginning of the 20th century, but surface plasmons that give rise to this kind of dichroism were firstly experimentally discovered in 1958 by Ritchie *et al.* Today, the unique optical properties of metallic nanoparticles enable a wide range of applications, such as light guiding, biodetection, enhanced optical transmission through sub-wavelength apertures, and optical imaging below the diffraction limit. [8, 24]

2.2.1 Surface Plasmons

Materials in the nanometer size regime have unique properties due to their high surface-to-volume ratio, quantum size effect, and electrodynamic interactions [25]. A metal nanoparticle can be considered as a resonator for surface plasmons, and therefore the resonating amplitude can locally exceed the exciting electromagnetic field by orders of magnitude. The quasi-free electrons in the ground states of metals behave as plasma, gas of free charge carriers. As the nanoparticles are exposed to an external oscillating field, the plasma begins to oscillate. The quanta of these longitunal electromagnetic charge density waves of this plasma are called plasmons. Generation of a plasmon is illustrated in Fig. 5. Surface plasmons play a significant role in metallic nanoparticles with sizes in the range of the penetration depth of an electromagnetic field into the metal on a wide range of frequencies. [8, 25]

The surface plasmons on metal nanoparticles (SPN) can be described theoretically in several ways. Mie-theory yields an exact analytical solution for scattering and absorption of light by spheres. This approach is explained in more detail in Sec. 2.2.2. For more complex systems, there are two good approximations: a quasistatic approximation and dipole approximation. In the quasistatic approximation, the exciting field is assumed to be homogeneous. Despite the simplifications made in the quasistatic approximation, it still takes into account the particle shape, the dielectric function of the metal and the dielectric function of the environment. The dipole approximation estimates the electromagnetic field of dipolar surface plasmon

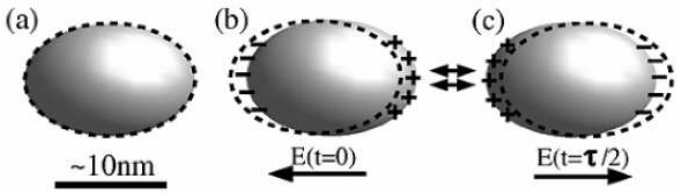

Figure 5: Generation of a plasmon on a metal particle under an external field (a) before exposure (b) at the beginning of a phase and (c) in the middle of an oscillation. [8]

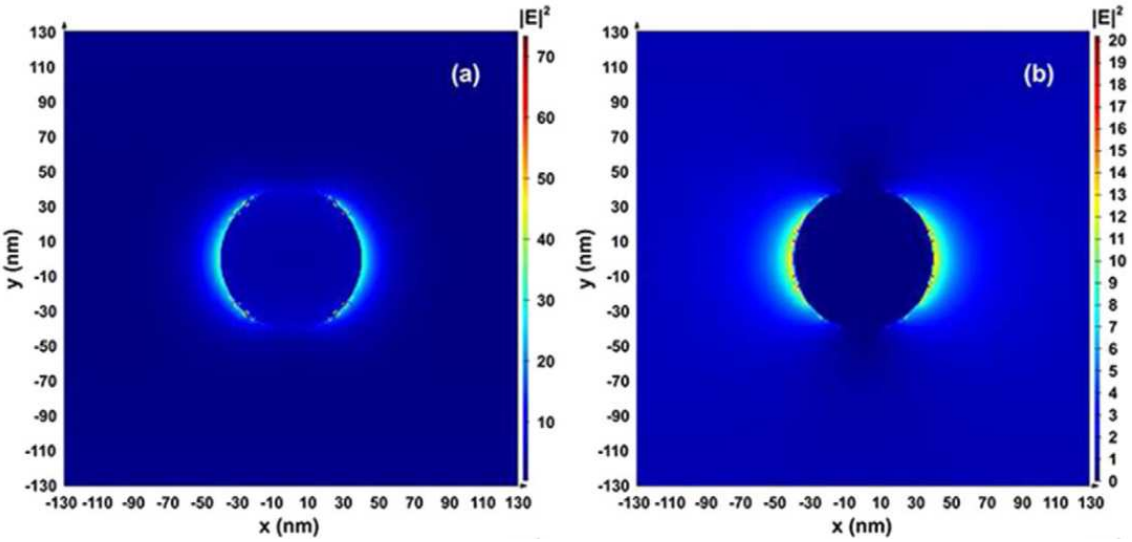

Figure 6: The distribution of electric field around a silver particle calculated by three-dimensional finite difference time domain method. A spherical silver nanoparticle of 80 nm in diameter excited by light with wavelengths of (a) 457 nm and (b) 820 nm. [26]

modes to be an electromagnetic field generated by an oscillating dipole at the center of a particle, neglecting the higher order oscillations. This approximation, also referred as Rayleigh approximation, is sufficient for particles with radius of R much smaller than the wavelength of the incident light λ, i.e. $2R << \lambda$, so that the interaction is governed by electrostatics instead of electrodynamics. This approximation reveals two spatial domains of the generated field: the near field and the far field. The near field is an evanescent field that extends to distances that are smaller than the wavelength of the electromagnetic fields, and depends on distance r as r^{-3}. The far field consists essentially of spherical waves, and is proportional to r^{-1}. [8, 25]

Surface plasmon resonance (SPR) occurs as the plasma oscillation is in phase with the incident field. In Fig. 6 the distribution of electric fields around a silver nanoparticle of 80 nm in diameter are illustrated under illumination with two wavelengths [26]. Under excitation with a 457 nm beam, the nanoparticle creates an enhanced local field that represents a field of a dipole. With excitation by 820 nm, the dipole-like behaviour remains, but is significantly weaker. This is due to the wavelength of the exciting light being further away from that of the SPR of the particle. [26]

The spectral width and the amplitude of the SPR are influenced mostly by scattering and absorption of the plasmon. Pure dephasing of SPN is shown to be negligible [8]. Scattering can be also described as radiation damping, where the electromagnetic waves are re-radiated from the SPN charge distribution. Absorption is an ohmic internal loss mechanism, where the plasmon ceases to exist and the energy is transferred to heat. The quasistatic approximation together with the dipole model give simple equations to evaluate the damping mechanisms, absorption and scattering cross-sections C_{abs} and C_{scat}:

$$\begin{aligned} C_{\text{abs}} &= k\text{Im}(\alpha_p) \\ C_{\text{scat}} &= \tfrac{k^4}{6\pi}|\alpha_p|^2, \end{aligned} \tag{1}$$

where α is the complex polarizability of the particle and k is the wave-number. Since the polarizability is proportional to the particle volume, the SPN damping mechanism is mainly governed by the particle size; for small particles, absorption is the dominating mechanism and scattering for larger particles. This leads to absorption on wider spectra for large particles compared to smaller particles. [8]

2.2.2 Mie Theory

Mie theory is an all-analytical theory of light scattering from a spherical particle. The theory was firstly presented by Gustav Mie in 1908, as he explained the red color of gold nanoparticles in a solution [25, 27]. The derivation of Mie efficiencies starts from Maxwell's equations in spherical coordinates. The configuration of the incident field with the electric and magnetic field components of the particle are defined by Helmholtz's equation. The Mie efficiencies Q_i, where i stands for extinction (ext), absorption (abs), scattering (sca) represent the extinction, absorption, and scattering coefficients for Helmholz's equation. They can be expressed in terms of scattering coefficients as [28]

$$Q_{sca} = \frac{2}{x^2}\sum_{n=1}^{\infty}(2n+1)(|a_n|^2 + |b_n|^2) \tag{2}$$

$$Q_{ext} = \frac{2}{x^2}\sum_{n=1}^{\infty}(2n+1)\text{Re}(a_n + b_n), \tag{3}$$

where a_n and b_n are the scattering coefficients for spherical particles when certain boundary conditions are applied. Energy conservation also requires that

$$Q_{ext} = Q_{sca} + Q_{abs}, \tag{4}$$

which makes it straightforward to calculate the absorption coefficient also. According to Mätzler [28], a_n and b_n are of the form

$$a_n = \frac{m^2 j_n(mx)[xj_n(x)]' - j_n(x)[mxj_n(mx)]'}{m^2 j_n(mx)[xh_n^{(1)}(x)]' - h_n^{(1)}(x)[mxj_n(mx)]'} \tag{5}$$

$$b_n = \frac{j_n(mx)[xj_n(x)]' - j_n(x)[mxj_n(mx)]'}{j_n(mx)[xh_n^{(1)}(x)]' - h_n^{(1)}(x)[mxj_n(mx)]'} \tag{6}$$

when $\mu = 1$, j_n are first kind spherical Bessel functions, and and $h_n^{(1)}$ are spherical Hankel functions. These spherical functions can be expressed with first kind Bessel functions $J_{n+1/2}$ and second kind Bessel functions $Y_{n+1/2}$ as

$$j_n(z) = \sqrt{\frac{\pi}{2z}}J_{n+1/2}(z),\ h_n^{(1)}(z) = j_n(z) + i\sqrt{\frac{\pi}{2z}Y_{n+1/2}(z)}. \tag{7}$$

The summation index n corresponds to the oscillation mode order, and $n_{\max}$ is defined as $n_{\max} = x + 4x^{1/3} + 2$. This has turned out to be a good guess for high enough summation index required for the sum to reach the convergent value with high enough accuracy. [27, 28, 29, 30]

2.3 Plasmon-Azo Interactions

The interaction between SPR and azobenzenes has been studied increasingly in recent years. The most probable mechanisms for SPN and azobenzene to interact are by heating effects or through the isomerization speed. There are many applications in materials science based on the pure heating effect of metal nanoparticles [31, 32]. However, the typical inscription intensities in the studies related to the light-induced phenomena of azobenzene molecules, are chosen to be in the range of 10 to 1000 mW/cm^2. For the applications that rely on the heating effect, typical intensities are $10^3 - 10^6$ W/cm^2, and the temperature is reported to increase only a few kelvins [31]. Therefore, it is more interesting to approach the problem through the isomerization speed.

It has been shown that photoisomerization quantum efficiency (PQE), the ratio of the number of isomerizations and the number of absorbed incident photons, can be manipulated by metallic nanostructures. In the studies by Xu *et al.* [33], gold films with a particle size of 10 nm, 30 nm, and 50 nm were prepared, along with a gold island film with approximately 30 nm island size. They showed, that the PQE is affected in two ways: the exciting pump field is enhanced by SPR, and the presence of gold particles accelerate the decay of the excited molecules from *cis* to *trans* form. The PQE can be modified precisely by adjusting the interparticle distance. The azobenzene dye used in the experiments was Disperse Red 1 (DR1). The absorption spectra of DR1 films did not differ, whether they were on a pure glass film or on a gold coated film. The PQE was improved only with the DR1 on a gold island film, and with the films consisting of nanoparticles, the efficiency was suppressed by larger nanoparticle size. [33]

A recent study by Yoon *et al.* shows that photoisomerization of azobenzene derivates induces a change in the aggregation state of metallic nanoparticles [34]. The gold nanoparticles used in the experiments were 33 ± 8 nm in diameter, which absorb strongly at 530 nm. However, increasing the amount of azobenzene derivatives[4] caused the sample absorbtion band to form a new peak near 700 nm, which slowly red-shifted during irradiation with UV light (365 nm). [34]

The effect of metallic nanoparticles on the photo-induced molecule reorientation in azobenzene-containing polymers has also been studied [36, 35, 37]. A study by Wu *et al.* demonstrates increased stability in birefringence writing-erasing cycles as silver nanoparticles are introduced in the azopolymer matrix [35]. Another study by Shen *et al.* demonstrates that the introduction of silver nanoparticles has a different effect in different azo-polymer matrices: for a polymer matrix containing azobenzene with a -CH_3 group the polymer orientation increased, and for a polymer

[4] 4-butyl-4'-(11-dodecylthioundecyloxy)-azobenzene

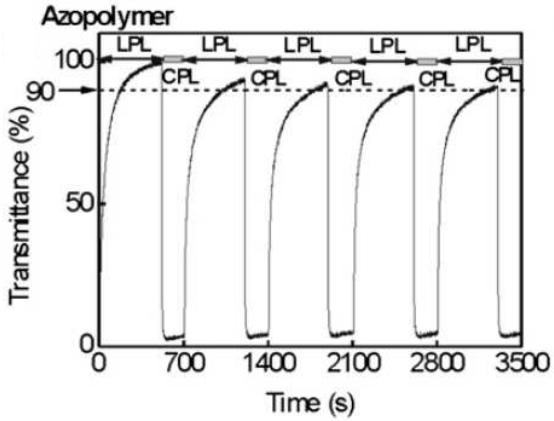

Figure 7: Relative transmittance of an azobenzene film as a function of time during five writing-erasing cycles. LPL stands for irradiation with linearly polarized light and CPL for irradiation with circularly polarized light. [35]

matrix containing azobenzene with a -CN group the polymer orientation decreased as the nanoparticle concentration increased [37]. Enhancement in photo-alignment has also been observed by introducing semiconductor particles instead of metallic nanoparticles in the material [38].

The addition of metallic nanopaticles to a polymer matrix has also other benefits. Since aggregation may be a problem with azobenzene chromophores with large permanent dipole moments, silver nanoparticles have been shown by Franco *et al.* to inhibit aggregation of dipolar chromophores more efficiently than organic inhibitors [39]. As aggregation inhibitors, the silver nanoparticles should be larger than the aggregating molecules. In the studies by Franco *et al.*, particles of 70.5 nm in diameter were used. Due to the large polarizability of silver, the amount of non-aggregated molecules was increased by 30% [39]. It was also noted that an excessive increase of silver nanoparticles could lead to the nanoparticles aggregating themselves. The usage of enhanced localized fields near the nanoparticles to enhance the optical responses of the chromophores was also suggested but not studied further. [39]

Promising results have been obtained with photopolymerization of composite materials when using metallic nanoparticles to enhance the irradiation field locally [40]. In the studies by Goldenberg *et al.*, 1.5 wt-% of gold nanoparticles (ca. 2 nm in diameter) were introduced in a composite system[5] in order to promote monomer spatial segregation. In the studies, the rate of photopolymerization was decreased along with the increased nanoparticle content in the composite. The resulting nanocomposite was also tested for holographic applications, such as SRG. The results show unusually high amplitude of the refractive index modulation in both the diffraction volume gratings and the polymerization rate. [40]

The link between the light-induced phenomena and plasmonics can also be thought from a completely other direction. Instead of harnessing plasmonic struc-

[5]ethoxylated bisphenol A diacrylate (EBPDA) and isooctylacrylate (IOA)

tures to enhance the SRG isncription process, periodic structures of SRGs can be utilized to manufacture different kinds of plasmonic structures. In studies by Moerland *et al.* plasmonic arrays of gold islands were succesfully created with two orthogonally inscribed SRGs, gold deposition, and ion milling [41]. Interesting results have also been obtained by functionalizing silver nanoparticles with azobenzene molecules [42]. In the studies by Ahonen *et al.*, silver nanoparticles were linked with an azobenzene dithiol molecule. It was shown that the separation of the nanoparticles could be switched by the isomerization of the azobenzene, thus changing the plasmonic properties of nanoparticle clusters [42].

3 Mie Efficiency Calculations

For a theoretical background, Mie efficiencies in an absorbing medium are calculated as a function of wavelength for spherical metallic nanoparticles with diameters of 8 nm, 30 nm and 50 nm. Firstly, the refractive index of the polymer matrix is resolved to define the wave vector inside the polymer matrix. That was done by fitting the absorption coefficient α with three Gaussian functions, since the overall absorption of the sample is a sum of the absorbing energy transitions in the molecules [43]. The three Gaussian functions represent the different energy transitions in the *trans* and *cis* states. Gaussian functions were used because the energy transitions of a molecule in a solid state experience a statistical distribution of environments [43]. The absorption coefficient is calculated from the absorption data of the used polymer-chromophore complex[6] by

$$\alpha = \frac{-log(10^y)}{z}, \tag{8}$$

where y is the absorption data and z is the film thickness. The absorption coefficient is related to the relative permittivity of the material ϵ_r by

$$\sqrt{\epsilon_r} = n + iK, \qquad \alpha = \frac{2\omega K}{c}, \tag{9}$$

where n and K are the real and imaginary parts of the refractive index of the material, ω is the angular frequency of light and c the speed of light in vacuum. Since the imaginary part of the refractive index is known, the real part can be estimated using Kramers-Kronig relations [44]. To do so, a MATLAB-function `kkrebook.m` was applied. The `kkrebook.m` uses a vector of the frequency components, ω, and a vector of the imaginary part of the permittivity under examination, K, as inputs, and they were defined from known data as

$$K = \lambda\frac{\alpha}{4\pi}, \qquad \omega = \frac{2\pi c}{\lambda}. \tag{10}$$

Since the refractive index is derived from the absorption data using Kramers-Kronig relations, one should note that the obtained values for n should actually be interpreted as a deviation in the refractive index in the observed region. It is reasonable to approximate the baseline for the refractive index to be that of a similar polymer. Since the refractive index of pure 4VP is 1.549 [45], the baseline is chosen to be 1.5. The values of the deviations in n and K are illustrated in Fig. 8(a).

In order to solve the Mie efficiencies, the permittivity of silver has to be known as a function of the wavelength. This is done by a MATLAB function `eps_BB.m` by Rakic *et al.* [46]. The real and imaginary parts of the relative permittivity of silver are illustrated in Fig. 8(b). With the now known values, a MATLAB function `mie.m` by Mätzler [28] will calculate the Mie efficiencies that represent the interaction cross sections C_i normalized to the particle cross section

[6] Explained in more detail in Sec. 4.1

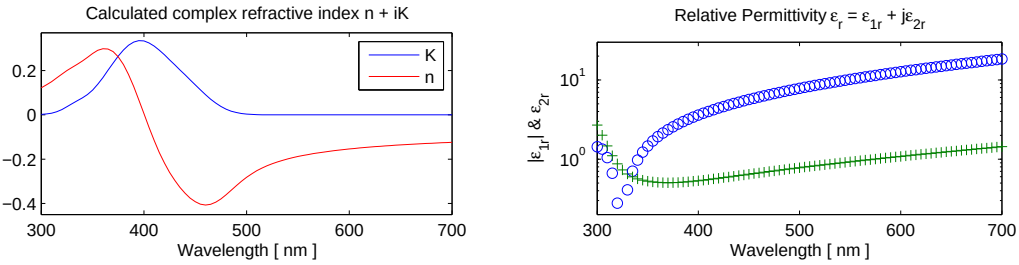

(a) (b)

Figure 8: (a) Deviation of the refractive index n (red) based on the imaginary part K (blue) due to absorption in the medium. (b) Real (blue) and imaginary (green) parts of the relative permittivity of silver.

$$Q_i = \frac{C_i}{\pi R^2}, \tag{11}$$

where i stands for extinction (ext), absorption (abs), and scattering (sca). The script `mie.m` uses Equations (2)-(7). The script was modified to calculate the Mie efficiencies as a function of wavelength. The Mie efficiencies Q_{ext}, Q_{scat} and Q_{abs} with three different particle sizes are illustrated in Fig. 9. The figures show that as the particle size increases, also the extinction efficiency term increases. However, also the scattering efficiency increases, which according to Equation (4) means that the absorption coefficient will decrease.

What also can be seen from Fig. 9, is the red shift of the plasmon resonance peak as the particle size increases. This is one of the reasons to use larger nanoparticles; to fit the plasmon resonance wavelength to match the irradiation sources available.

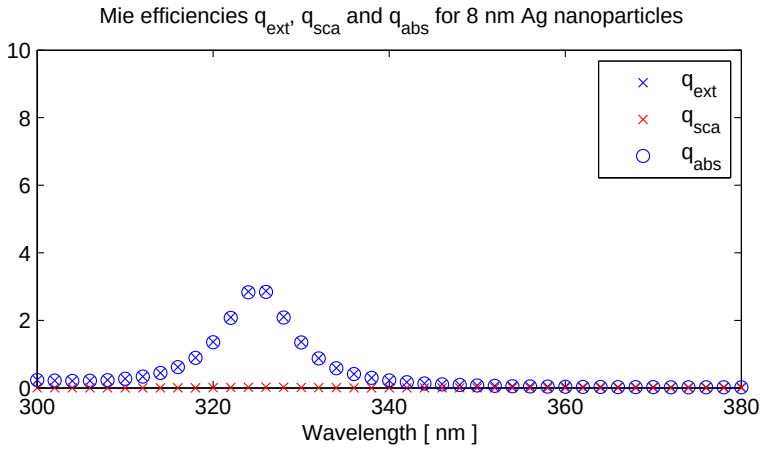

(a)

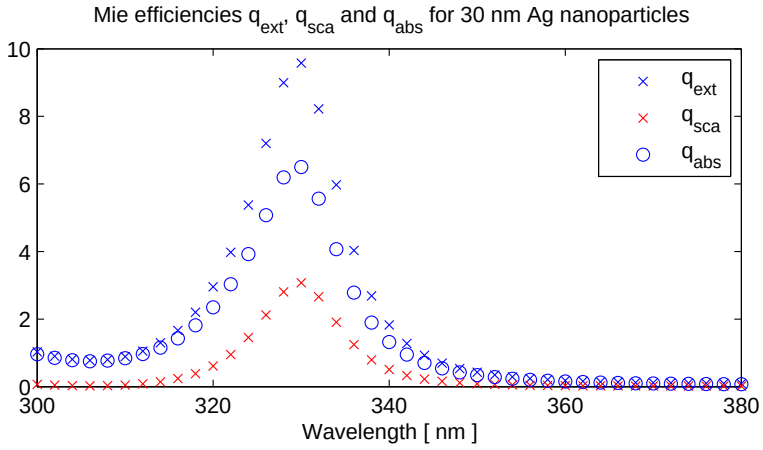

(b)

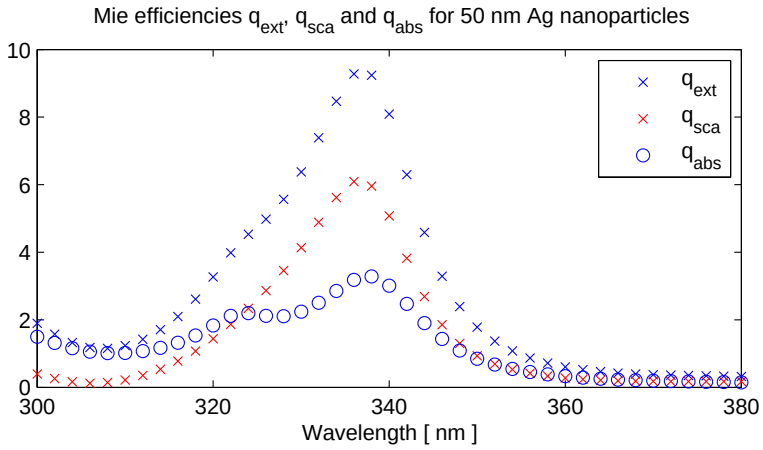

(c)

Figure 9: The Mie efficiencies q_{ext} and q_{sca} of silver nanoparticles of (a) 8 nm (b) 30 nm and (c) 50 nm in diameter.

4 Experimental Setups and Methods

In this section, the sample preparation methods, the sample compositions, and the experimental setups used in the measurements are explained. Finally, the methods used for imaging the structures are presented briefly.

4.1 Sample Preparation

In order to study the dynamics and stability of light-induced properties in azobenzene-containing materials, it is most convenient to make thin films. The material is chosen so that the absorption of the material's *trans* and *cis* states lie at the visible range of the spectrum and the maximum absorption of the material would be close to the SPR frequency of the used nanoparticles. The thin films are made on a transparent substrate to minimize influence of the substrate to the transmission of the sample, since most of the experimental measurements are obtained from the transmission side of the sample. Because the SRG can reach modulation depths of several hundred nanometers, the thin films should be thick enough so that the thickness will not influence on the SRG formation process. In order to obtain comparable results, the thin films should also be of the same thickness with respect to each other.

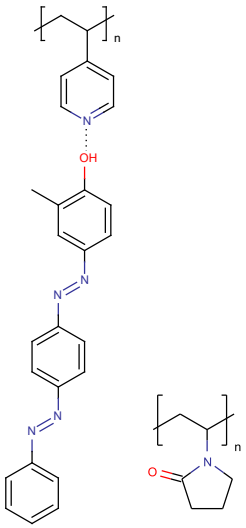

(a) (b)

Figure 10: Chemical structure of (a) p4VP(DY7)$_{1.0}$ complex and (b) PVP repetition unit.

The polymer used was poly(4-vinylpyridine) (p4VP)[7] and the chromophore was a bisazobenzene molecule with two azo-bonds, Disperse Yellow 7 (DY7)[8] that has an absorption maximum at $\lambda_{max} = 385$ nm. The chromophore can be classified as an aminoazobenzene by its spectral properties, even if it lacks the amino group and thus is structurally closer to an azobenzene-type molecule. The polymer was provided by Polymer Source and the chromophore by Sigma-Aldrich. The chromophore is linked to the polymer via hydrogen bonding [47]. The chemical composition of the used materials is presented in Fig. 10(a). The complexation ratio 0.5 stands for the relative amount of chromophores with respect to the repetition units of the polymer; every other repetition unit of the polymer is hydrogen-bonded with a chromophore. Even if the introduced silver nanoparticles would decrease the chance of aggregation of the surrounding medium, the complexation ratio was fixed to 0.5, for it has shown to be the most efficient complexation ratio for this polymer-chromophore combination in SRG formation [47].

[7] $M_w = 5,406$

[8] 2-Methyl-4-[(E)-4-[(E)-phenyldiazenyl]phenyldiazenyl]phenol

Table 1: Sample details, the precise Ag/Complex mass ratios, film thicknesses h, estimated interparticle distances d.

Sample	Precise Ag-%	h (nm)	d (nm)
SRG - 8 nm particles			
p4VP(DY7)$_{0.5}$	0	230	∞
p4VP(DY7)$_{0.5}$+0.5% Ag 8nm	0.71	-	73.4
p4VP(DY7)$_{0.5}$+1.0% Ag 8nm	1.05	220	64.5
p4VP(DY7)$_{0.5}$+1.5% Ag 8nm	1.52	-	57.0
p4VP(DY7)$_{0.5}$+3.0% Ag 8nm	3.15	230	44.7
p4VP(DY7)$_{0.5}$+5.0% Ag 8nm	5.26	230	37.7
p4VP(DY7)$_{0.5}$+7.5% Ag 8nm	7.66	235	33.2
p4VP(DY7)$_{0.5}$+10.0% Ag 8nm	9.94	210	30.5
SRG - Wavelength comparison			
p4VP(DY7)$_{0.5}$	0	238	∞
p4VP(DY7)$_{0.5}$+0.5% Ag 30nm	0.51	245	307.5
p4VP(DY7)$_{0.5}$+1.0% Ag 30nm	1.01	330	244.9
p4VP(DY7)$_{0.5}$+1.5% Ag 30nm	1.45	356	217.1
p4VP(DY7)$_{0.5}$+2.0% Ag 30nm	1.99	277	195.3
p4VP(DY7)$_{0.5}$+0.5% Ag 50nm	0.62	258	480.2
p4VP(DY7)$_{0.5}$+1.0% Ag 50nm	1.06	333	401.6
p4VP(DY7)$_{0.5}$+1.5% Ag 50nm	1.49	320	358.5
p4VP(DY7)$_{0.5}$+2.0% Ag 50nm	1.97	340	326.6
SRG, birefringence and *cis* lifetimes			
p4VP(DY7)$_{0.5}$	0	255	∞
p4VP(DY7)$_{0.5}$+0.5% Ag 30nm	0.51	265	307.5
p4VP(DY7)$_{0.5}$+1.0% Ag 30nm	1.08	225	239.5
p4VP(DY7)$_{0.5}$+1.5% Ag 30nm	1.60	220	201.1
p4VP(DY7)$_{0.5}$+2.0% Ag 30nm	2.04	250	193.7
p4VP(DY7)$_{0.5}$+0.5% Ag 50nm	0.59	245	488.2
p4VP(DY7)$_{0.5}$+1.0% Ag 50nm	1.05	255	402.9
p4VP(DY7)$_{0.5}$+1.5% Ag 50nm	1.59	260	350.8
p4VP(DY7)$_{0.5}$+2.0% Ag 50nm	2.14	220	317.8

In the beginning, silver nanoparticles with diameter of 8 nm were used. The particles were synthesized by a two phase method [42]. Inspired by the calculations described in Sec. 3, larger particles were ordered from nanoComposix. The motivation to use silver nanopaticles was that silver has the lowest losses in the visible spectrum, and the surface plasmon resonance of silver nanoparticles overlaps the absorption of the used chromophore [24]. The particles were delivered with a polyvinylpyrrolidone-coating (PVP) that allowed good colloidal stability and a solubility in polar organic solvents. The specification sheets for the ordered particles can be found in Appendix A.

All starting materials were used as received, dissolved in chloroform[9] and then mixed to give the nominal complexation ratios described in Table 1. From the

[9] $CHCl_3$

solutions, thin films were prepared by spin-coating on quartz substrates. The thicknesses of the films were confirmed with a DEKTAK32 profilometer. The exact AgNP/complex ratios, thin film thicknesses h and estimated interparticle distances in the samples are presented in Table 1. The average distances between particles were approximated by a simple cubic lattice, which is commonly done in literature [48, 49].

4.2 Experimental Setups

In the experimental setups two irradiation beams are used, one at 457 nm[10] and another at 405 nm[11]. The quality of the 457 nm Ar^+ laser beam is improved by using a spatial filter in order to remove aberrations from the beam. In a spatial filter, the beam is focused through a pinhole, creating a pattern similar to a two-dimensional Fourier transform of the beam's transverse intensity distribution. This filtering technique is often called Fourier-filtering. The polarization of the irradiation laser beam is adjusted with wave-plates. Wave-plates introduce a controlled phase shift between the polarization components of the beam. A half-wave-plate introduces a phase shift of π, and a quarter-wave-plate introduces a phase shift of $\pi/2$ between the polarization components of the incident light for corresponding wavelengths λ. Thus a half-wave-plate was used to control the linearly polarized light and a quarter-wave-plate to create a circularly polarized light. The laser beam used for irradiation with light of a wavelength of 405 nm was not Fourier-filtered in order to obtain reasonably high irradiation intensities.

4.2.1 UV-Vis Spectra

Plenty of useful information can be obtained purely from the absorption spectrum of a film. Since the absorption peak of the chromophore and the expected resonance frequency of the particles are both in the visible region of the spectrum, the spectra were taken over a range of 300 nm to 600 nm. The spectrometer used for the experiments was a λ950 from PerkinElmer. The spectra are obtained in the transmission mode, and thus they include also the reflection from the material surface. The absorption value of 1 stands for 10% of relative transmission through the sample. The absorption coefficient can be derived by Equation (8).

4.2.2 Surface-Relief Gratings

A Lloyd-mirror setup provides a method to create a sinusoidal 1-D interference pattern with a grating period ranging from few hundred nanometers to several microns. The working principle of the setup is illustrated in Fig. 11. The sample is placed perpendicular to the reflecting mirror so that half of the irradiation beam propagates directly to the sample surface, and half via a reflection from the mirror. The mod-

[10] Ar^+ laser, Coherent Innova 70

[11] Solid-state laser, CrystaLaser, DL_405-040-SO

ulation period of the formed interference pattern on the sample surface, Λ, depends on the wavelength of the irradiation beam, λ, and the incident angle, θ, by

$$\Lambda = \frac{\lambda}{2 \sin \theta}. \tag{12}$$

The incident angle θ is the angle between the inscription beam propagation vector and the normal of the sample plane. All the measurements in this thesis were done with a grating period of 1 μm, and the incident angle was set according to Equation (12).

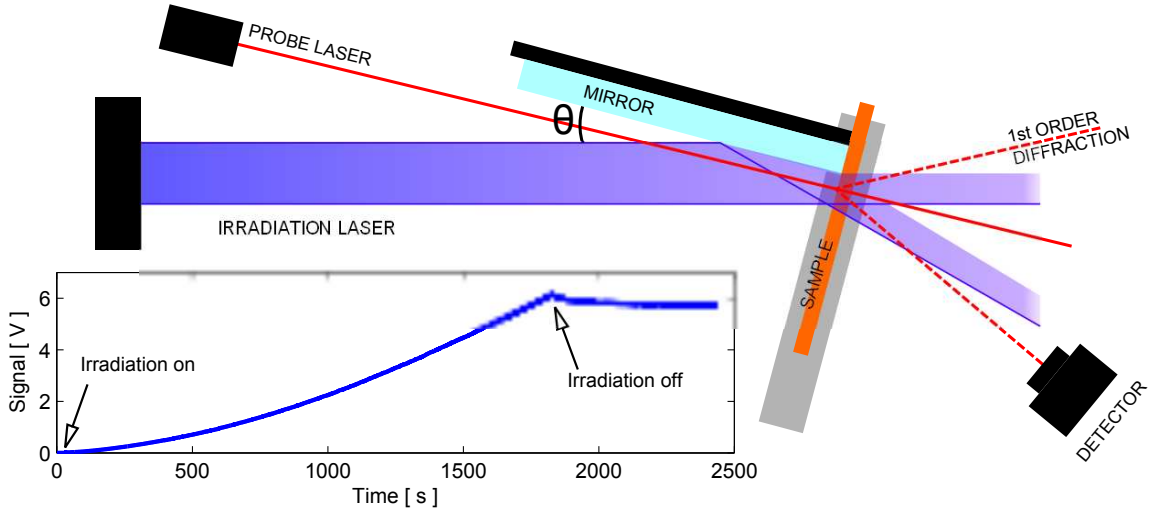

Figure 11: Schematic of a Lloyd mirror setup used for SRG formation. Half of the irradiation beam is reflected from the mirror on the sample surface creating an interference pattern with the other half of the beam, which propagates directly to the sample. The 1st order diffraction of a separate probe beam from the forming SRG is recorded to observe the dynamics of the SRG formation. Inset: Typical signal obtained from the photodetector.

As discussed in Sec. 2.1.3, the surface mass transport depends on the polarization of the incident light. In the experiments, a p-p polarization geometry was used, despite the fact that with the materials used in the literature, stronger surface-relief gratings have been obtained with a circularly polarized inscription geometry [3]. The inscription geometry with linear polarization was chosen, since the induced plasmons would resonate in the direction of the polarization component of the incident field. Circularly polarized irradiation was assumed to create weaker enhancement in the local field induced by the SPR in the direction of the grating vector.

The formation of the SRG was monitored using a separate laser beam, aligned to penetrate the sample in the direction of the normal of the sample plane. The wavelength of the probe beam should be chosen so that it is not absorbed by the chromophores. This probe laser diffracts from the grating with a strength, which depends on the modulation depth of the grating [47]. The irradiation of the sample was stopped before a saturation point of the SRG formation. A typical signal obtained from the photodetector during the irradiation and SRG formation is illus-

trated in the inset of Fig. 11, where also the beginning and the end of the irradiation are marked.

4.2.3 Birefringence

The light-induced birefringence is observed from the samples using the setup illustrated in Fig. 12. The irradiation beam is fixed to s-polarization, so that the choice of the incident angle of the irradiation beam would not affect the results. The inscription intensity is lower than in the SRG inscription process in order to obtain reliable data also during the fast increase of the birefringence in the beginning of the exposure. The polarization of the probe beam is controlled with a polarizer, and another polarizer is used as an analyzer. The polarizers are crossed and fixed to $\pm 45°$ with respect to the inscription beam, so that transmission through anisotropic material would give a minimum signal on the detector. The probe beam, as it is polarized at 45° with respect to the optical axes of the material before the sample, has a polarization component along both the ordinary and extraordinary optical axes. During the irradiation, the molecules in the sample reorientate as explained in the Sec. 2.1.2, which can be detected as increased transmission on the detector. A quarter-waveplate is included to the setup in order to create a circularly polarized beam from the inscription beam, which can erase the formed anisotropy on the sample. The behaviour of the signal in different stages of the birefringence inscription-erasure process are illustrated in the inset of Fig. 12.

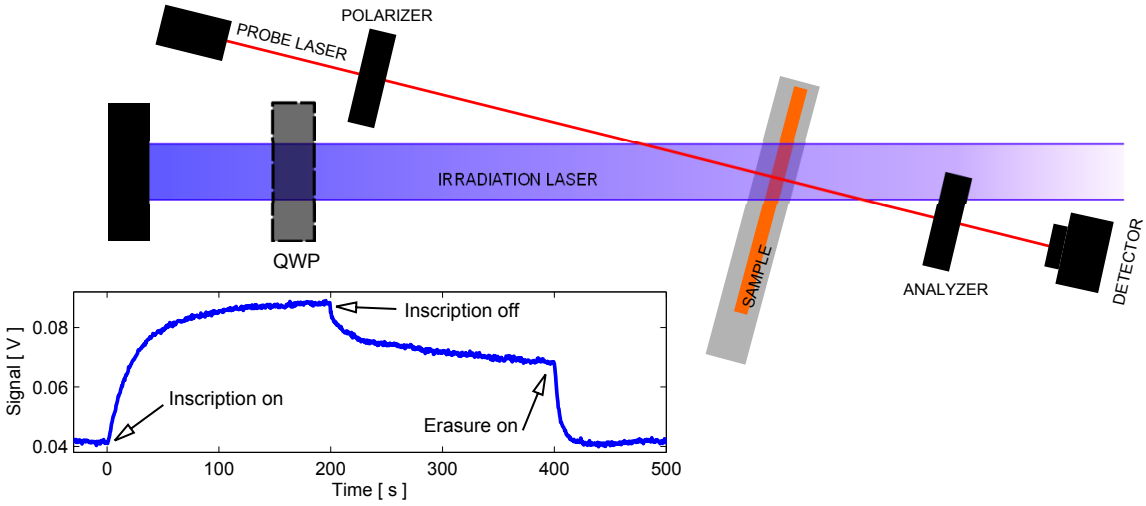

Figure 12: Schematic of a setup used for birefringence inscription. The orientation of the azobenzene molecules is detected as a change in transmission of a separate probe beam through crossed polarizers. Inset: A typical signal obtained on the photodetector.

The birefringence, i.e., the difference in the refraction indices of the material for the ordinary and extraordinary optical axes, is defined as $\Delta n = n_o - n_e$ and can be calculated from

$$I = I_0 \sin^2\left(\frac{\pi|\Delta n|h}{\lambda}\right), \tag{13}$$

where I is the signal from the detector, I_0 is the transmitted signal propagating through the sample in an isotropic state and parallel-aligned polarizers, h is the film thickness and λ is the wavelength of the probe beam. The dynamics of the birefringence formation during the exposure is studied by observing the time constants of a biexponential fit. After reducing background noise from the data, the fitting equation can be expressed as

$$\Delta n = A_1(1 - e^{-t/\tau_1}) + A_2(1 - e^{-t/\tau_2}), \tag{14}$$

where τ_1 and τ_2 are the time constants and A_1 and A_2 are amplitudes of the fitting curves [50].

4.2.4 *cis*-Lifetime Measurements

The *cis*-lifetimes of the chromophores are measured with a setup illustrated in Fig. 13. As a white light source, a xenon lamp was used and filtered with a 420 nm band-pass filter[12], which corresponds to the *trans* absorption band. The sample was exposed to a circularly polarized laser beam (405 nm). As the *cis* concentration increases, the transmission of the 420 nm light increases until a photo-stationary state is reached. After that, the exposure with the 405 nm beam is stopped, and the transmission decreases as the chromophores relax thermally to the *trans* state.

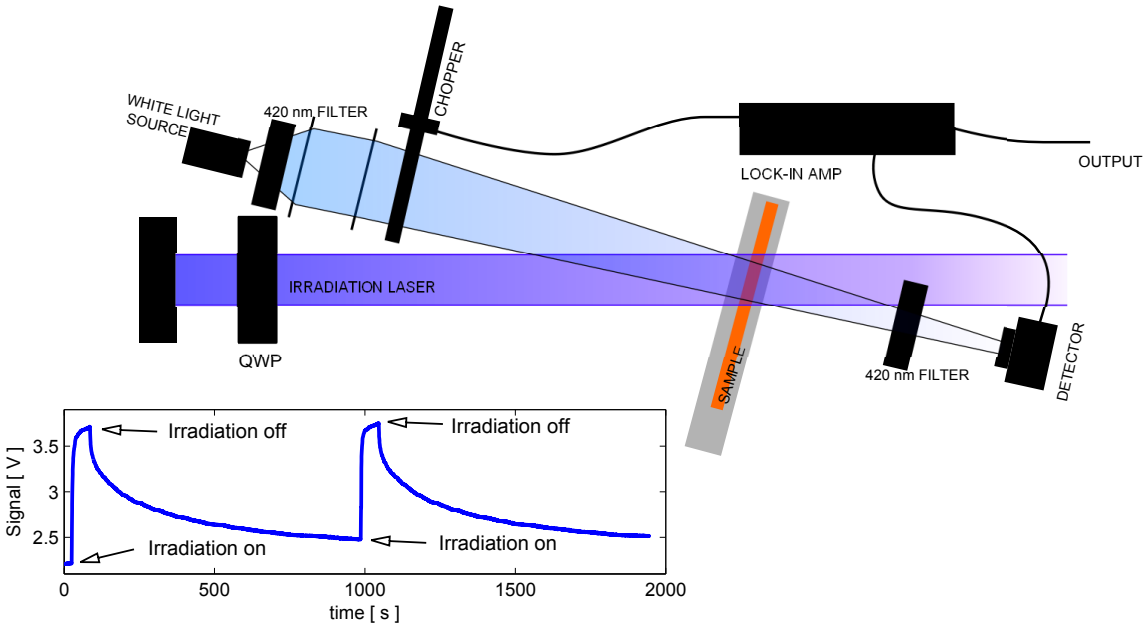

Figure 13: Schematic of a *cis* lifetime setup. The *cis* isomer concentration is detected as change in the transmission of the probe beam through the sample. A spectrally filtered white light source is used as a probe. The signal is amplified by a lock-in amplifier. Inset: A typical signal obtained from the amplifier as a function of time during two exposure cycles.

[12]Center wavelength: 420 ± 2 nm, Full width at half maximum: 10 ± 2 nm

Since the signal from the filtered white light source is so small, the signal-to-noise ratio was improved by a lock-in amplifier. The measured signal was chopped into pulses with a chopper. The lock-in amplifier uses the chopping frequency as a trigger to integrate the signal over several pulses, thereby reducing the noise. In the measurements, the chopper frequency is set to 200 Hz and the lock-in time constant to 100 ms. The intensity of the 405 nm irradiation beam is 150 mW/cm^2. An example of a *cis* lifetime measurement data as a function of time is illustrated in the inset of Fig. 13. As can be seen from the figure, the measurement is cycled twice for each sample. In each cycle, the sample was exposed to the incident beam for 60 seconds with a proper relaxation time after the exposure (900 s or 600 s).

The *cis*-lifetimes are obtained from the absorption coefficients of the samples according to a method introduced by Barrett *et al.* [51]. Since the setup measures the transmission, the absorbances are calculated form the equation

$$I = I_0 e^{-A} \Rightarrow A = -\ln(I/I_0) \tag{15}$$

where A is the absorbance of the sample, I is the signal, and I_0 is the transmission of the recording beam through a plain substrate. The first order *cis-trans* thermal isomerization is denoted by a time constant k_t as

$$k_t[cis] = -d[cis]/dt = d[trans]/dt. \tag{16}$$

By assuming a completely reversible isomerization, all the molecules are at the *trans* state after infinitely long period of relaxation. The absorbance of the film is then given by the sum of the absorbances of the isomers:

$$A = A_{cis} + A_{trans}. \tag{17}$$

The absorbances of the *cis* and *trans* isomers are given by

$$A_{cis} = \alpha_c[cis]_0 e^{-k_t t}, \qquad A_{trans} = \alpha_t[[trans]_\infty - [cis]_0 e^{-k_t t}], \tag{18}$$

where α_c and α_t stand for the absorbances of the isomers at the probe wavelength. The absorbance of the film is thus given by

$$A = A_\infty - (\alpha_t - \alpha_c)[cis]_0 e^{-k_t t}, \tag{19}$$

and the time constant k_t can be interpreted as a slope of a linear fit from a plot of $ln(A_\infty - A)$. The *cis* lifetime is the reciprocal of k_t. [51]

4.2.5 Nanomicroscopy

In order to analyse the samples, two imaging methods are used. Firstly, the inscribed SRGs are imaged by atomic force microscopy (AFM). The atomic force microscopy is based on a moving tip on top of the sample surface. This method gives accurate information about the sample topology, and thus the main motivation to use AFM for imaging the samples is to obtain the modulation amplitudes of the SRGs. The AFM images are taken from a 10 μm $\times$ 10 μm area, and with a grating period of

$\Lambda = 1$ μm, ten periods are captured on each image. From these, an average over five modulations is used to estimate the modulation depth of the whole grating. An axample of an AFM image taken from a SRG is illustrated in Fig. 14 along with a graph of a typical surface profile of a SRG. The AFM used for imaging is a Multimode Dimension 5000 in the NanoMicroscopy Center, operated in tapping mode.

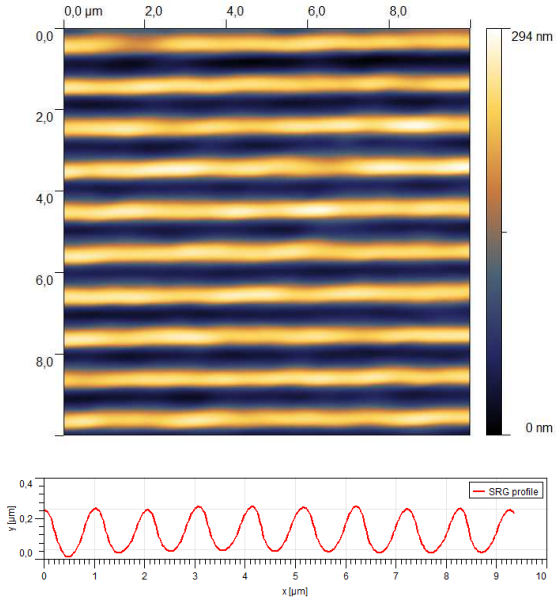

Figure 14: An example image of a SRG obtained by AFM and a surface profile of SRG.

Another imaging method that was used is scanning electron microscopy (SEM). The motivation to use SEM images is to get information about the distribution of the silver nanoparticles on the surface of the sample after the inscription of the SRGs. Before imaging, the samples are coated with a thin layer of metal in order to avoid electron charging during the imaging. A metal layer of gold palladium is made by sputtering. The SEM used for the imaging was JEOL JSM-7500F in the NanoMicroscopy Center.

5 Results and Discussion

This section presents the results of the experiments performed in this thesis. It is divided into three subsections according to the set of prepared samples.

5.1 8 nm Particles

The SRG inscription results with 405 nm on samples containing 8 nm silver particles revealed promising results in enhancing the inscription process. The 1st order diffraction efficiencies and the modulation depths of the inscribed SRGs as a function of the Ag/complex mass ratio are illustrated in Fig. 15. The inscription time for the samples was 600 seconds. The figure shows that the 1st order diffraction efficiencies are greater with AgNP/complex ratios of 0.5% - 1.5% than for the sample without AgNPs. The samples with 0.5% and 1.5% of AgNPs were prepared after the rest of the series, and therefore are not completely comparable with the other samples of the series due to the possible oxidation of the particles. However, the results indicate that an increasing use of nanoparticles leads to a weakening of the diffraction efficiency and the inscription process. With lower concentrations of AgNPs, the modulation depths are mostly unaffected by the particles, but decrease as the nanoparticle concentration exeeds 5 wt-%.

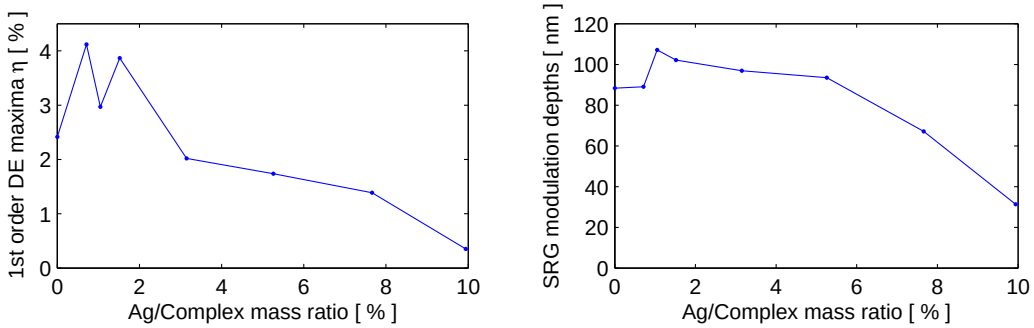

(a) (b)

Figure 15: (a) 1st order diffraction efficiencies and (b) modulation depths as a fuction of Ag/complex mass ratio for p4VP(DY7)$_{0.5}$ + 8 nm particles. Lines are drawn to guide the eye. (p-polarized, 405 nm 130 mW/cm^2, 600 s irradiation)

Even if both the diffraction efficiencies and grating modulation depths after irradiating the samples with 405 nm laser light for 600 seconds are higher for the samples containing moderate amounts of nanoparticles than for those without particles, the values of the diffraction efficiencies are surprisingly low for the measured samples. As a side result from the measurements, it was noticed the age of the sample affects the inscription process. This is most likely due to the oxidation of the nanoparticles. The following measurements were performed as soon as possible after the sample preparation.

5.2 Wavelength comparison

The SRG inscription on samples containing particles of 30 nm and 50 nm in diameter was executed with two wavelengths, 405 nm and 457 nm. The 1st order diffraction efficiencies and the modulation depths of the inscribed SRGs as a function of Ag/complex mass ratios and estimated interparticle distances are illustrated in Fig. 16. With Ag/complex mass ratios ranging from 0.5% to 2.0%, the estimated interparticle distances with 30 nm particles range from 195 nm to 307 nm and with 50 nm particles from 326 nm to 480 nm. These distances cover the inscription wavelength and half of the inscription wavelength on both of the used wavelengths. As can be seen in Fig. 16(a), there is a decreasing trend of the diffraction efficiency as a function of the silver nanoparticle concentration with both of the wavelengths and both of the particle sizes with a few minor exceptions.

The most interesting exceptions to the decreasing trend in the diffraction efficiencies are in samples containing 0.5 wt-% of AgNPs of 30 nm in diameter, where the diffraction efficiencies exceed the values of those without AgNPs. In Fig. 16(b) are the modulation depths of the inscribed SRGs as a function of the Ag/complex mass ratio. In the modulation depths, the decreasing trend is not as clear. Instead,

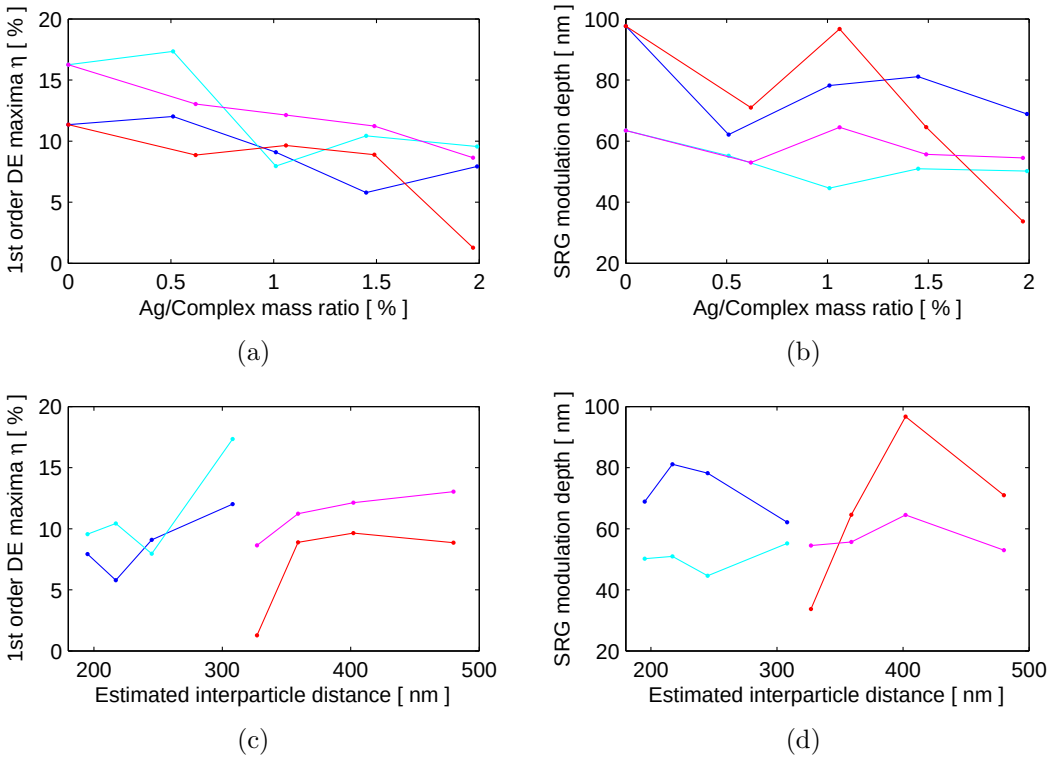

Figure 16: 1st order diffraction efficiencies and modulation depths as functions of interparticle distances and Ag/complex mass ratios for p4VP(DY7)$_{0.5}$ + 30 nm and 50 nm particles. Lines are drawn to guide the eye. (Irradiation: p-pol, 405 nm 150 mW/cm^2 or 457 nm 100 mW/cm^2, 800 s) **Blue: 30 nm, 405 nm; Cyan: 30 nm, 457 nm; Red: 50 nm, 405 nm; Magenta: 50 nm, 457 nm.**

there is a significant peak in the modulation depths in the samples with 1 wt-% of 50 nm AgNPs. With the potential error in the modulation depth measurements in mind, the modulation depths of these two SRGs do not exceed the modulation depths of those without AgNPs.

The same results from Figs. 16(a) and 16(b) are plotted as a function of interparticle distances in Fig.s. 16(c) ans 16(d). Interestingly, as can be seen in Fig. 16(d), even if the SRG modulation depth is not greater than in the sample without the nanoparticles, the highest modulation depth in the samples with the nanoparticles is achieved when the interparticle distance is similar to the inscription wavelength, which is roughly the same as the wavelength of the SPR.

Another interesting detail when comparing Figs. 16(c) and 16(d), is the behaviour of the samples containing 30 nm particles when irradiating with 405 nm light. The less efficient diffraction effiency appears to result in a deeper modulation depth. This is most likely due to the scattering effect of the AgNPs, which makes less intensity of the probe beam to propagate to other direction orders than the first one.

From these result it can also be seen that greater modulation depths and a more clear dependence on the particle concentration are obtained with the wavelength of 405 nm. This is one of the main motivations to study the light-induced phenomena in more detail using the 405 nm irradiation.

5.3 SRG Formation and Birefringence with 405 nm Irradiation

5.3.1 Spectral Properties and SRG

The absorption spectra of the p4VP(DY7)$_{0.5}$ thin films containing 0 – 2 wt-% of silver nanoparticles of 30 and 50 nm in diameter are presented in Fig. 17. The shape of the absorption spectrum does not change significantly with the AgNP concentration, but a clear decrease in the overall absorption of the material can be observed as the AgNP concentration increases. Since there are no clearly observable peaks in the absorption spectra at the wavelength of the SPR of the AgNPs, the absorption values at the overall absorption maxima are investigated in more detail. The absorption values of the samples at the absorption maxima as a function of the Ag/complex mass ratio are presented in Fig. 18(a). The absorption maxima show a clear decreasing trend in the absorption of the samples. Whereas the absorption peak for the sample containing no AgNPs shows an absorption value of ca. 1.7, in the samples containing 2 wt-% of AgNPs the absorption has decreased to a value of ca. 1.2.

Another interesting outcome from these spectra is the shift in the absorption wavelength as a function of the AgNP concentration. Even though the shift is relatively small, it can easily be distinguished from the data taken in the intervals of 0.25 nm. The wavelengths, in which the absorption maxima occur, as a function of the Ag/complex mass ratio are presented in Fig. 18(b). In the case of 30 nm particles the red-shift reaches its maximum value at the Ag/complex mass ratio

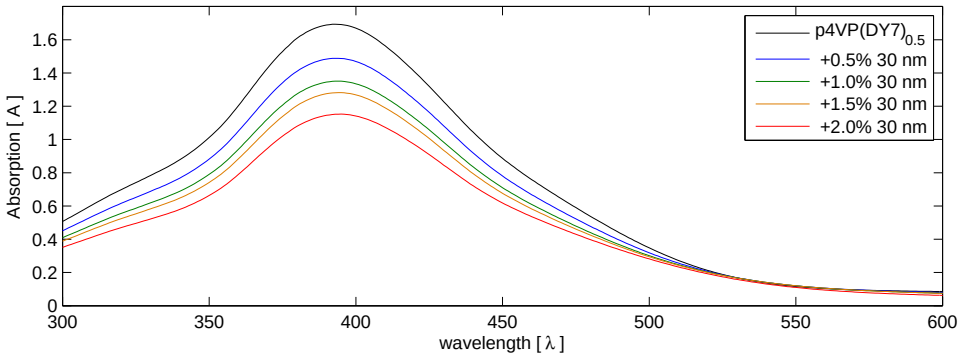

(a)

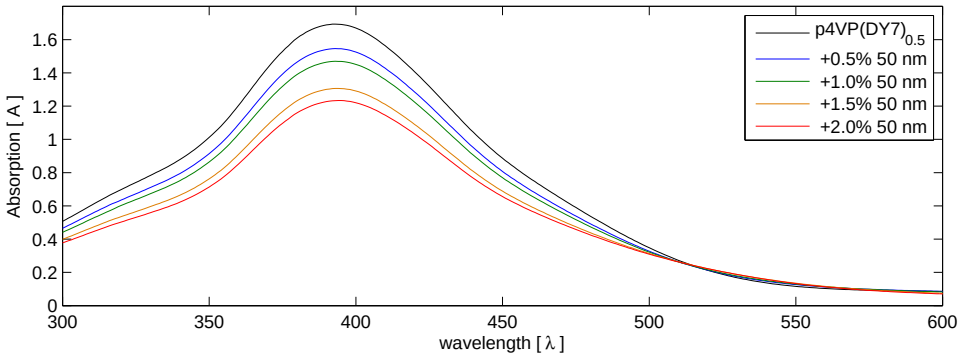

(b)

Figure 17: Absorption spectra of the p4VP(DY7)$_{0.5}$ samples containing AgNPs (a) 30 nm and (b) 50 nm in diameter.

of 1.5 wt-%, but decreases for the sample containing 2.0 wt-% of AgNPs. In the samples containing 50 nm AgNPs, the influence of the AgNP concentration to the absorption maximum wavelength is more moderate.

The reason for the significant decrease in the absorption maximum with the

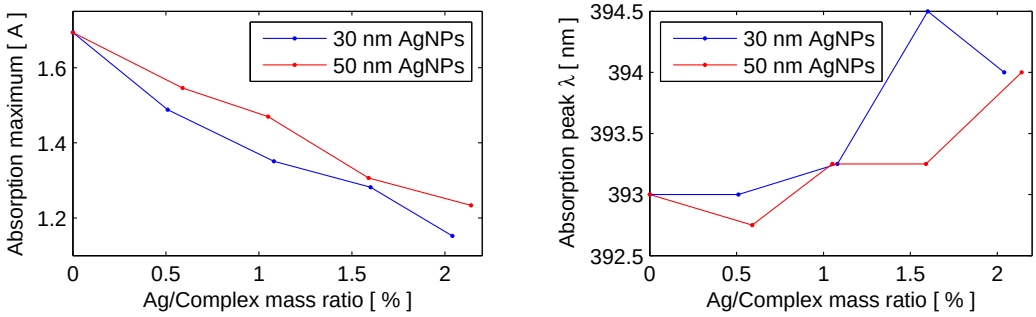

(a) (b)

Figure 18: (a) The maxima of the absorption spectra and (b) the wavelength at which it occurs as a function of Ag/complex mass ratio. Lines are drawn to guide the eye.

increase of AnNP concentration is unclear. Since the absorption spectra in all the samples were of similar shape with that of the sample containing no AgNPs, the SPR can be said to have no influence to the spectral properties of the material. However, introducing the AgNPs in the material could change the effective refractive index of the material, and thus increase the reflection in the measurements. Also, the PVP coating on the nanoparticles could have an effect on the spectral properties of the material, but the coating only can not solely be responsible for such a significant change in the absorption. It must also be noted that the roughness of the sample surface, which also could contribute to the scattering, was not studied in detail.

The inscriptions of SRGs reveal reasonable results. The dynamics of the SRG inscription process was expected to show differences between the samples, but the real time measurements of the first-order diffraction efficiencies presented in Fig. 19 do not reveal such differences. The SRG inscription was executed as described in Sec. 4.2.2. From the Figure it can clearly be seen that the inscription has started at 30 s and ended 1800 s after the beginning of the irradiation. There is also a relaxation phase after the inscription that is due to the chemical relaxation in the polymer matrix. The diffraction efficiency values are clearly decreasing as the AgNP concentration increases. The maximum 1st order diffraction efficiency values as a function of the Ag/complex mass ratio are discussed later in the text.

The first seconds of the inscription are shown in Fig. 20 in more detail. The rapid increase of the diffraction efficiency in the initial state of the SRG inscription process is due to the formation of photochemical and orientational gratings. The formation of these weakly diffracting gratings depends on the polarization state of the probe laser, and requires significantly smaller time scales to occur. A small decrease in the diffraction efficiency after the rapid increase in the beginning occurs, because the other gratings are out of phase with respect to the SRG, as explained in Sec. 2.1.3. The polarization of the probe laser was not changed between the samples in order to keep the initial behaviour in the diffraction efficiencies comparable with each other.

The maximum diffraction efficiencies, as the samples were irradiated for 1800 seconds, are illustrated in Fig. 21(a). The diffraction maxima of the last measurement series reveal a diminishing influence of the nanoparticles to the diffraction efficiencies, without exceptions. The diffraction efficiency values are significantly smaller than in the previous measurements, even though the irradiation intensity was only 10% weaker. The reason for this difference is most likely in the tuning of the setup between the inscriptions. The whole series was made under exactly similar conditions, so the results within the series are comparable. The maximum diffraction efficiency in the sample containing no AgNPs is significantly higher than in those with added AgNPs. The increased amount of AgNPs leads to a decrease in the diffraction efficiencies after irradiation for 1800 s. The diffraction efficiency of the samples containing 2 wt-% of AgNPs decreases by a factor of 3 with respect to the sample containing no AgNPs. This occurs with both 30 nm and 50 nm nanoparticles.

Figure 21(b) shows the 1st order diffraction efficiency maxima at the initial stage of irradiation as a function of Ag/complex mass ratio. From the figure it can be

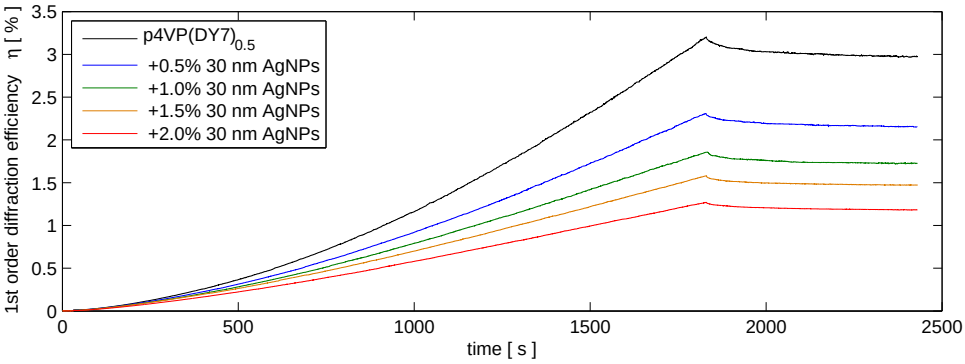

(a)

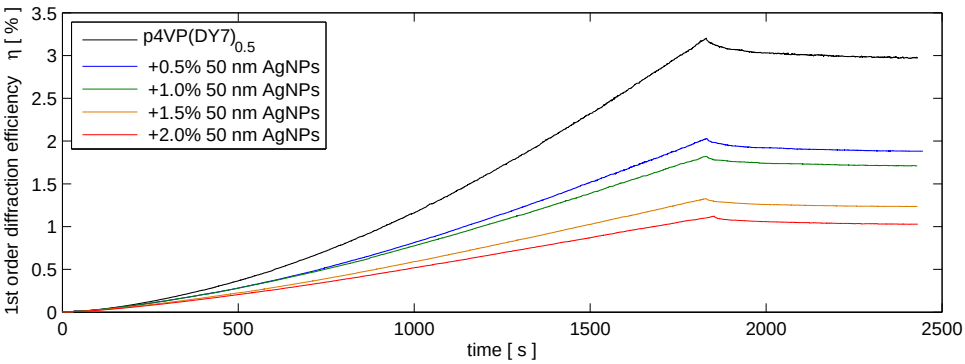

(b)

Figure 19: 1st order diffraction efficiencies of the p4VP(DY7)$_{0.5}$ samples containing AgNPs (a) 30 nm and (b) 50 nm in diameter during irradiation. Irradiation: 405 nm, p-polarized, 135 mW/cm^2, 1800 s.

clearly seen that also the diffraction due to the formation of other types of gratings is affected by the AgNPs in a similar way. The decrease is slightly stronger with the samples containing 30 nm particles than with those containing 50 nm particles. The samples with a Ag/complex mass ratio on 2 wt-% show a decrease by a factor of 2 in the samples with 30 nm particles, and by a factor of 1.5 in the samples with 50 nm particles.

As stated in Sec. 4.2.2, in a regular case, the probe laser would diffract more from the grating with a higher modulation depth. As can be seen in Fig. 22 by comparing it to Fig. 21(a), the modulation depths of the gratings do not coincide entirely. With the 50 nm silver nanoparticles, the trend of the modulation depths is decreasing, apart from a slight increase in the modulation depth between the samples with Ag/complex mass ratios of 0.5% and 1.0%. With 30 nm nanoparticles, the decrease is dramatic until 1.0% of AgNPs, where the modulation depth of the SRG is less than half of that of the sample containing no AgNPs. With larger amounts of 30 nm AgNPs, the modulation depths become deeper.

The behaviour of the SRG modulation depths and the 1st order diffraction efficiencies differ significantly from each other in the samples containing 30 nm nanopar-

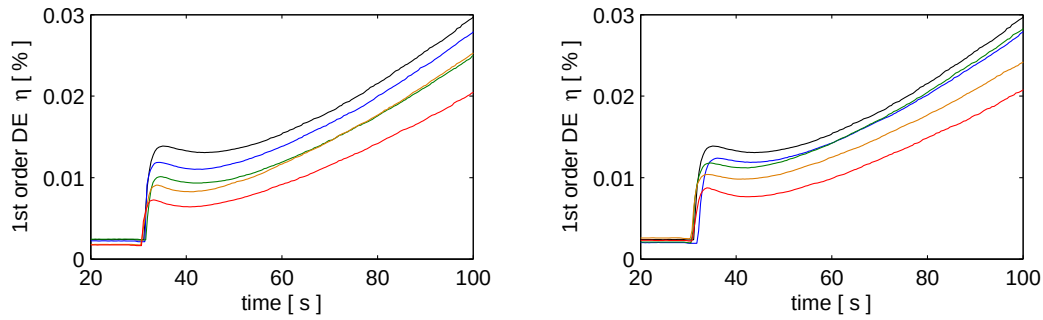

(a) 30 nm AgNPs (b) 50 nm AgNPs

Figure 20: 1st order diffraction efficiencies of the p4VP(DY7)$_{0.5}$ samples containing AgNPs (a) 30 nm and (b) 50 nm in diameter during the beginning of inscription. Irradiation: 405 nm, p-polarized, 135 mW/cm^2. The colour codes are the same as in Fig. 19.

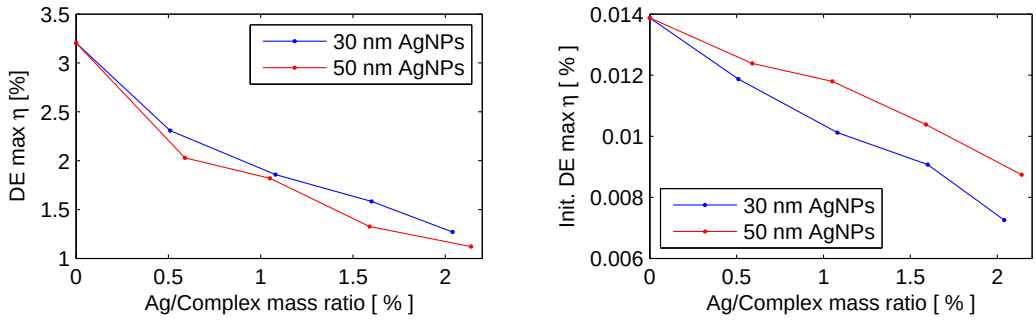

(a) (b)

Figure 21: The maxima of the 1st order diffraction efficiencies (a) at 1800 seconds of irradiation and (b) at the initial stage of irradiation as a function of Ag/Complex mass ratio. Irradiation: 405 nm, p-polarized, 135 mW/cm^2. Lines are drawn to guide the eye.

ticles. The measurement made for the wavelength comparison in similar samples did suggest an interesting behaviour, when the estimated interparticle distance approaches half of the SPR wavelength of the nanoparticles. Also in the final measurements, the SRG modulation depth is increased at the corresponding Ag/complex ratio, but continues to increase at the Ag/complex ratio of 2% again. This behaviour would suggest either a change in the plasmonic properties of the particles due to aggregation or oxidation of the particles, or a decrease in the amount of nanoparticles due to the sample preparation procedure.

The samples were imaged by scanning electron microscopy (SEM) in order to examine the nanoparticle distribution on the sample surface after SRG inscription. At first, the samples were imaged as such, but the quality of the SEM images was highly distorted due to the charging of the electrons on the surface of the non-conducting sample. The samples were then coated by sputtering with a thin metal layer, a layer of gold palladium, in order to make the sample surface conducting to avoid the charging. The images taken of the sputtered SRG structures are presented in Fig. 23. The imaged sample was a p4VP(DY7)$_{0.5}$ film doped with 1.5 wt-%

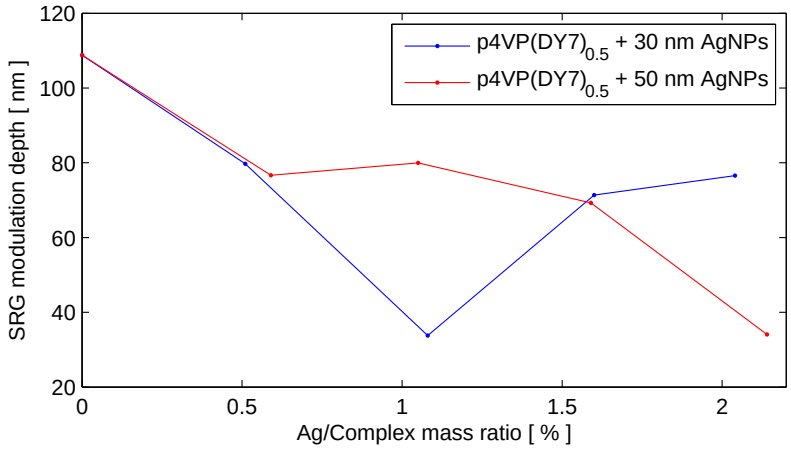

Figure 22: SRG modulation depths after 1800 s of irradiation (405 nm, p-polarized, 135 mW/cm^2) as a function of the Ag/complex mass ratio. Lines are drawn to guide the eye.

of 30 nm AgNPs. The grating was inscribed with 405 nm p-polarized beam for 1800 s. In the sample, the estimated interparticle distance is ca. 200 nm, so the particles should be clearly visible in the images. In Fig. 23(a) the SRG is imaged with a magnification of 6,500, and the grating can be clearly seen as a periodic structure on the sample surface. In Fig. 23(b) the grating is imaged in more detail, with a magnification of 90,000. Despite the good quality of the image, no silver nanoparticles can be distinguished from the image, which is most likely due to the thin metal coating.

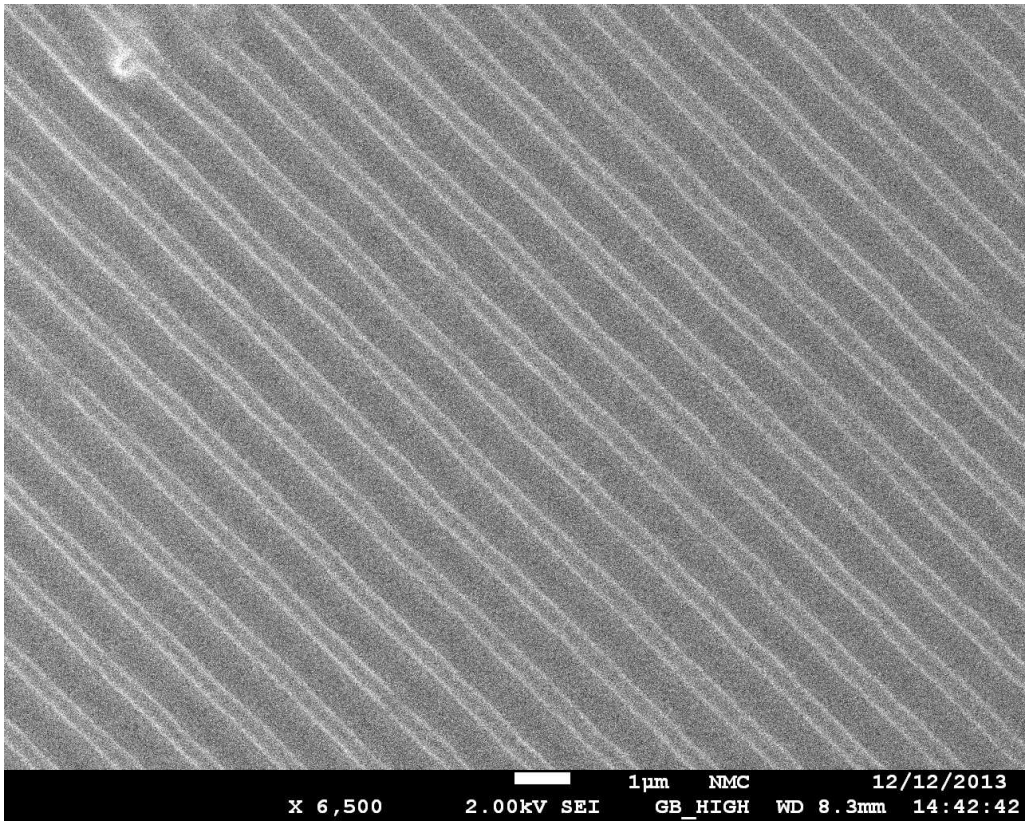

(a)

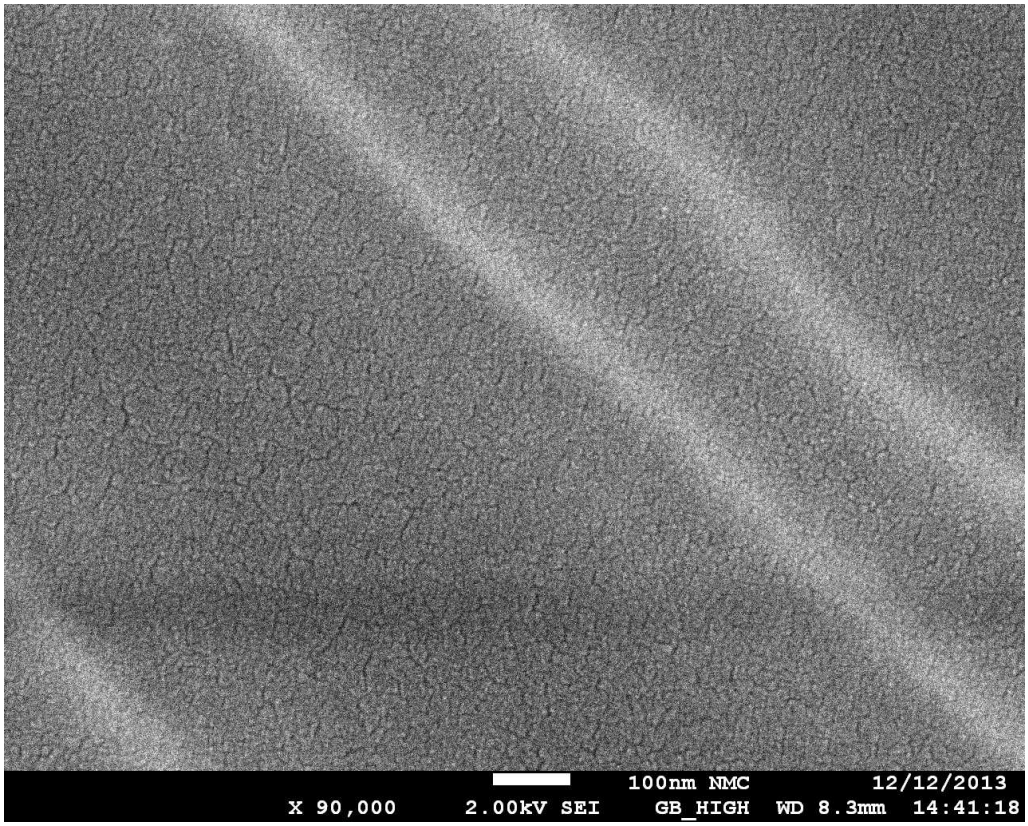

(b)

Figure 23: A SEM image of a SRG sputtered with gold palladium with a magnification of (a) 6,500 and (b) 90,000. The metal layer is visible, but no nanoparticles can be seen.

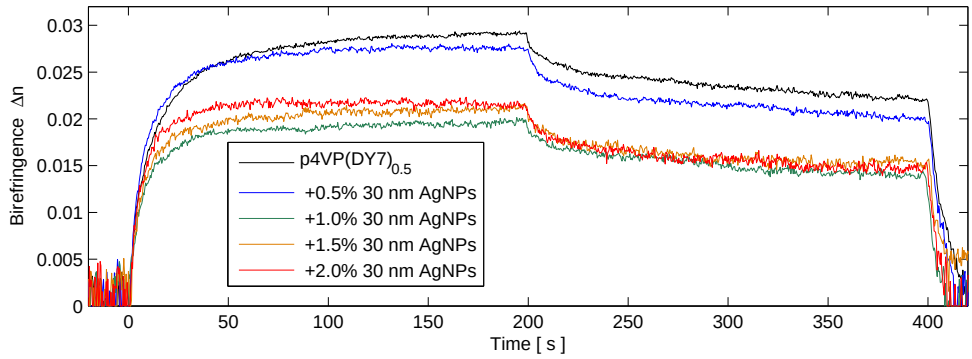

(a)

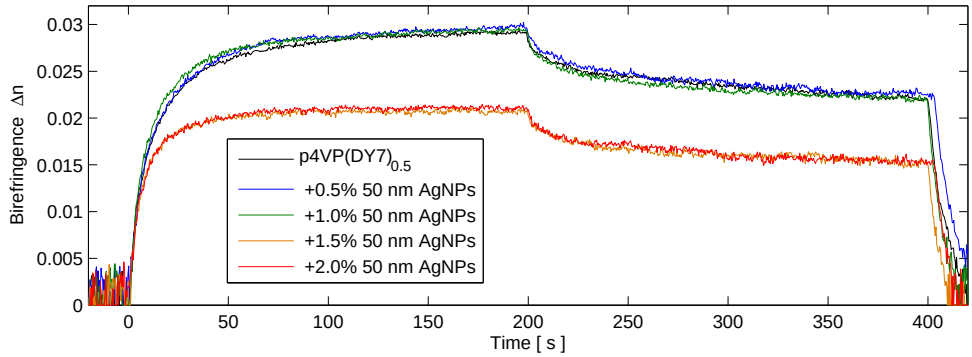

(b)

Figure 24: Birefringence of the p4VP(DY7)$_{0.5}$ samples containing AgNPs (a) 30 nm and (b) 50 nm in diameter during irradiation. Irradiation: 405 nm, 50 mW/cm^2.

5.3.2 Birefringence and *cis* lifetimes

The photo-induced birefringencies of the samples as a function of time of inscription with 405 nm (50 mW/cm^2) are illustrated in Fig. 24. The figure shows the behaviour of the birefringence as the irradiation begins at 0 s, is stopped at 200 s, and an erasure with circularly polarized beam begins at 400 s. From this figure, one can note that the birefringence is not significantly influenced by the amount of AgNPs until a certain threshold concentration is reached.

This threshold-like behaviour as a function of AgNP content is examined in more detail in Fig. 25, where the maximum values of the birefringence measurements as a function of the Ag/complex mass ratio at the end of the inscription and before the beginning of the erasure are illustrated. The Figure shows that the threshold for 30 nm particles lies between Ag/complex mass ratios of 0.5% and 1%, and for 50 nm nanoparticles between 1% and 1.5%. The relaxed maxima in both cases follow the behaviour of the total maxima. Even if the samples with low concentrations of 50 nm AgNPs show slightly higher values of birefringence than those without AgNPs, the differences can be concidered negligible due to the possible error factors during the measurements.

The speed of birefringence formation in the sample is studied in more detail by

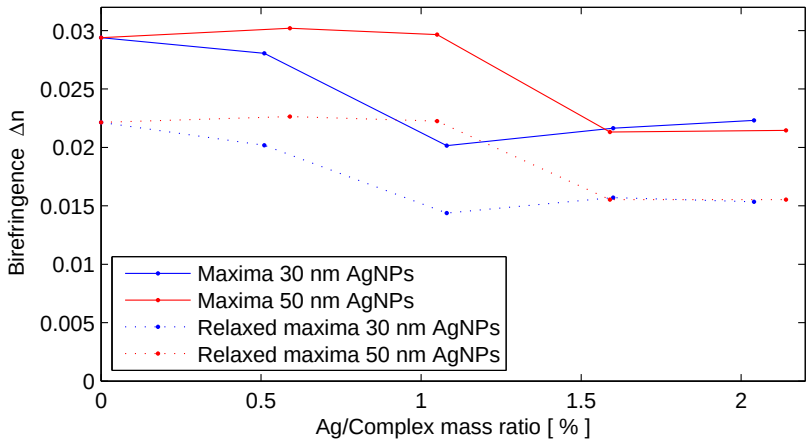

Figure 25: Birefringence maxima by function of Ag/complex mass ratio in the end of irradiation (solid lines) and before the erasure with circularly polarized light (dashed lines). Irradiation: 405 nm, 50 mW/cm^2. Lines are drawn to guide the eye.

making a biexponential fit (Equation (14)) to the data, where τ_1 and τ_2 are the time constants that can be interpreted to tell about the dynamics of the process. The amplitudes A_1 and A_2 are not of interest. The time constants τ_1 and τ_2 as a function of the Ag/complex mass ratio are plotted in Fig. 26. Both time constants show roughly the same kind of behaviour as a function of Ag/complex mass ratio. It can be noted that the birefringence inscription is slowest in the sample containing 1.5% of AgNPs of 30 nm in diameter. Unexpectedly, there is no clear correlation between the birefringence maxima of the samples and the time constants.

The strong decrease in the birefringence values for the samples with an increasing amount of 30 nm AgNPs at a Ag/complex mass ratio of 1.0% is similar to the decrease in the SRG modulation depth. This behaviour would suggest that with this amount of AgNPs, the orientation motion of the azobenzene molecules is suppressed. With 50 nm AgNPs, the suppression occurs at a slightly greater Ag/complex mass ratio. This could be due to a change in the plasmonic behaviour of the nanoparticles.

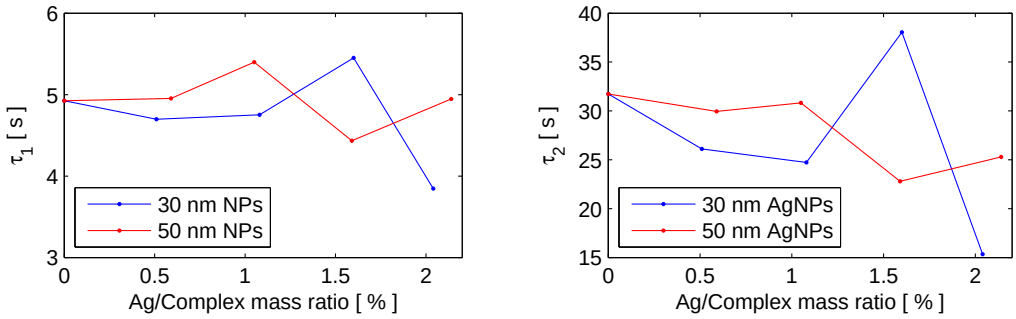

(a) (b)

Figure 26: Time constants of the birefringence measurements (a) τ_1 and (b) τ_2 according to Equation (14). Irradiation: 405 nm, 50 mW/cm^2. Lines are drawn to guide the eye.

However, the examination of the speed of the birefringence formation shows a peak in the time coefficients of the biexponential fits at Ag/complex mass ratios, for which the estimated interparticle distances are of the same order as the wavelength where SPR is to occur. These results also support the assumption that the molecular orientation is suppressed by the AgNPs at the SPR wavelength.

The *cis* lifetime measurements were made with a setup explained in Sec. 4.2.4. The *cis* lifetimes were obtained from the data by applying the Equation (19). A proper fit was made to the second relaxation slope of each piece of measurement data. The time constants k_t from the *cis* lifetime fits by a function of the Ag/Complex mass ratio are plotted in Fig. 27(a), and the corresponding *cis* lifetimes in Fig. 27(b).

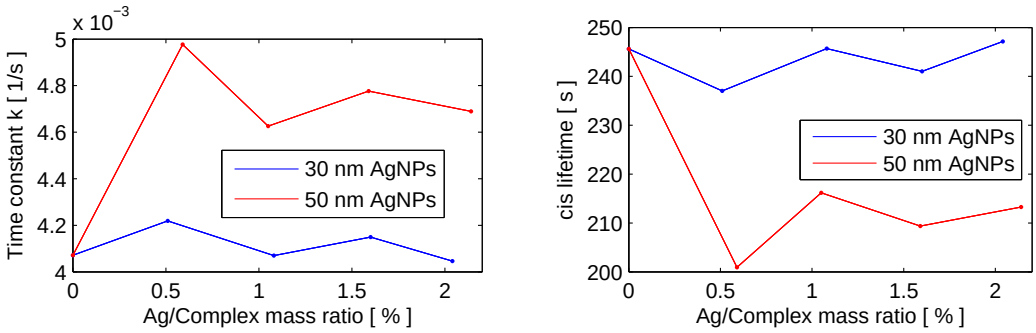

(a) (b)

Figure 27: a) Time constants k_t obtained from the *cis* lifetime measurements. (b) *cis* lifetimes as obtained by applying Equation (19). Lines are drawn to guide the eye.

In Fig. 27 one can see that the *cis* lifetimes are slightly increased with an increased amount of 30 nm AgNPs, but for 50 nm AgNPs the lifetimes become shorter. The *cis* lifetime is clearly shortest within the sample containing 0.5 wt-% of 50 nm AgNPs, in which the lifetime is decreased by more than 15%.

The increased *cis* lifetime in the samples containing 30 nm AgNPs supports the hyphothesis that the isomerization is stabilized by an increase of the amount of AgNPs. However, the changes in the *cis* lifetimes are so small that they could be considered negligible. The effect of 50 nm AgNPs, however, is significant. Even if the Mie efficiency of absorption for the 50 nm nanoparticles is smaller than for 30 nm particles, the decrease in the *cis* lifetimes is most likely due to the heating effect at the SPR. Even if the heating is only few kelvins, the probability for thermal back-isomerization from *trans* state to *cis* state will increase, and would lead to the observed behaviour.

6 Conclusions

In this thesis, light-induced motions were studied in azopolymer thin films doped with silver nanoparticles. For the thesis, calculations on the optical properties for silver nanoparticles of different sizes were made. Several methods to study the effect of the silver nanoparticle concentration on the light-induced phenomena in azopolymer-containing thin films were performed. The light-induced phenomena studied were photo-induced surface-relief grating (SRG) formation, photo-induced birefringence and the lifetimes of the metastable *cis* isomers of azobenzene molecules. In this section, conclusions are drawn from the main results. Finally, some points are suggested for future studies on the subject.

6.1 Methods

All the thin films used in the experiments were prepared by dissolving the materials in chloroform, and by spin-coating the films on quartz substrates from the solutions. The complexation ratios and Ag/Complex mass ratios were calculated according to the mass of the solution. Possible sources for error in the sample preparation come from the environment. The humidity in the laboratory does not remain constant throughout the year, which may lead to differences in the film quality between the sample series. Also, even if the silver nanoparticles had a PVP coating, there is a possibility of nanoparticle oxidation. All the solutions containing nanoparticles were sonicated for at least 15 minutes before use to avoid aggregation of the nanoparticles and to ensure as reliable values of nanoparticle concentration in the thin films as possible.

The inscription setups for photo-induced SRG and birefringence, as well as the setup for the *cis* lifetime measurements, required precise alignment of the optical components. Each component in the setup induces a possibility of error to the measurements. All the components were adjusted by hand, and some adjustments had to be made between the sample series. When interpreting the results, this has to be taken into account. The inscription process is also affected by the quality of the laser itself. The 405 nm laser was not Fourier-filtered in order to get a sufficient amount of intensity for the inscription. This may have an effect to the SRG quality, as well as to the molecular orientation. The errors caused by the setups are, however, considered small while making conclusions of the results.

For imaging, atomic force microscopy (AFM) and scanning electron microscopy (SEM) were used. The AFM was used mainly to obtain the modulation depths of SRGs. The quality of an AFM image depends on the quality of the probe tip, which was tested before every imaging session. The largest possible error in the AFM imaging comes from the imaging area selection. A perturbation in the irradiation setup may lead to an uneven quality of the SRG. In order to avoid the error due to AFM, each AFM image was taken from the same relative location of the SRG in each sample. In SEM images no nanoparticles were observed due to the thin metal layer, that was necessary to have in order to obtain images of good quality.

6.2 Results

The calculations of the Mie efficiencies for silver nanoparticles of different sizes quantify the effect of the size of the nanoparticle to its plasmonic behaviour. As the diameter of the nanoparticle increases, the plasmon resonance shifts towards longer wavelengths. On small particles, most of the interaction between the incident light and the nanoparticle is through absorption. On larger particles, scattering begins to dominate, i.e., the plasmonic properties of the particles will change towards the properties of bulk silver.

The inscription of SRGs on azobenzene-containing polymer films doped with silver nanoparticles of 8 nm in diameter revealed an increase in the SRG formation for modest AgNP concentrations. The increase was notable for both the 1st order diffraction efficiencies and the SRG modulation depths, as the Ag/complex mass ratio was less than 1.5%. The decrease of both the 1st order diffraction efficiency and the SRG modulation depths as the Ag/complex mass ratio exceeded 5% is most likely due to aggregation of the nanoparticles. Also, according to the Mie efficiency calculations, the plasmon resonance wavelength for 8 nm nanoparticles is ca. 360 nm. The effect could increase if the inscription wavelength and the wavelength of the chromophore absorbance would be closer to the plasmon resonance wavelength.

The plasmon resonance wavelength and the irradiation wavelength are closer when introducing larger nanoparticles. With the samples containing 30 nm and 50 nm silver nanoparticles, inscription of SRGs was executed with two wavelengths: 405 nm and 457 nm. The 1st order diffraction efficiencies and the modulation depths of the formed SRGs were examined as functions of Ag/complex mass ratios and estimated interparticle distances. With the larger particles no enhancement was observed in either diffraction efficiencies or modulation depths compared to those measured from the sample containing no nanoparticles. However, the effect of the particle concentration on the observed values was notably different for the two inscription wavelengths. Inscription with 405 nm on samples containing 30 nm particles did show that the diffraction efficiency and the SRG modulation depth do not correlate on these samples. Additionally, an increase in the modulation depth on samples that had an estimated interparticle distances of ca. the wavelength or half of the wavelength of the 405 nm irradiation light was observed. However, the diffraction efficiency was decreased with an increase in the nanoparticle concentration, which is most likely due to increased scattering from the large particles. Inscription with 457 nm resulted in smaller modulation depths and larger diffraction efficiencies, which was most likely due to the better quality of the 457 nm laser beam.

Further studies on the SRG inscription with the 405 nm laser revealed a dramatic decrease in the diffraction efficiencies as the nanoparticle concentration was increased for both the 30 nm and 50 nm silver nanoparticles. Again, the SRG modulation depths did not correlate with the diffraction efficiencies. A dramatic decrease of the SRG modulation depths was observed on samples containing 1 wt% of 30 nm nanoparticles. This change in the behaviour as compared to the previous set of measurements could be explained by a change in the plasmonic properties of the nanoparticles due to oxidation between preparation of the sample sets. Also, the

concentration of nanoparticles in the nanoparticle solutions may have been different, even if the possible error factors in the sample preparation were minimized by sonication prior to each step of sample preparation.

The inscription of photo-induced birefringence on samples containing larger nanoparticles showed that the maximum birefringence values were unaffected by the nanoparticle concentration until a certain threshold value for the nanoparticle concentration was reached. In the samples containing 30 nm silver nanoparticles, the threshold value lay between 0.5 and 1.0 wt-%, and for 50 nm silver nanoparticles between 1.0 and 1.5 wt-%, after which the maximum birefringence value was decreased. For the samples containing 30 nm nanoparticles, this threshold value corresponded to an amount of nanoparticles, which resulted also on the weakest SRG modulation depth. Examination of the dynamics of the birefringence formation revealed that on the samples containing 50 nm particles, the birefringence formation dynamics correlated to the maximum birefringence values. In case of the 30 nm nanoparticles, the speed of the birefringence formation was strongly decreased on the sample containing 1.5 wt-% of nanoparticles.

The *cis* lifetime measurements showed that the lifetime of the *cis* isomer of the azobenzene molecule was slightly increased as a function of the 30 nm silver nanoparticle concentration. However, the increase was so small that it could be estimated to be negligible. For 50 nm nanoparticles, even modest amounts of nanoparticles caused the *cis* lifetimes to decrease ca. 15%. The photochemical properties of the used chromophore make the interpretation of these results difficult, as in a bisazobenzene there are two isomerizable azo-bonds. One may, however, conclude that since the *cis* $\rightarrow$ *trans* isomerization is thermally metastable, even a small increase in the temperature could cause this kind of changes in the *cis* lifetimes.

6.3 Future Studies

As can be seen from the Mie efficiency calculations, the larger the particle, the stronger is the scattering, and thus the nanoparticles will begin to behave in a plasmonic manner. Combined with the rather unexpected results with 50 nm silver nanoparticles, a suggested conclusion is to keep the nanoparticles smaller than 50 nm in order to obtain as efficient local field enhancement as possible. Also, with smaller particles, smaller interparticle distances are obtained with the same mass ratios. This is desirable due to the short range of the local field enhancement.

Even if silver has rather small losses, i.e., the penetration depth is larger than, e.g., for gold, there are no clear benefits in using silver instead of gold regarding the enhancement of the light-induced phenomena on azobenzene-containing polymer films. Inspection of the optical properties of spherical metallic nanoscale particles through the Mie efficiencies reveal that the optimal conditions for SPR are with particles smaller than 30 nm in diameter. The plasmon resonance frequency is thus moved to the UV region. This is one of the reasons why it is recommended to use gold nanoparticles under 10 nm in diameter instead of silver, since the SPR resonance frequency would lie in the visible region of the spectrum, and would thus be more suitable to be used in azobenzene-containing systems.

As stated earlier, the aggregation of organic molecules can be prevented by inclusion of silver nanoparticles in the system. In the used chromophore-polymer combination, the optimal complexation ratio has been proven to be 0.5, which could be because of the aggregation of the chromophores or decreased free volume around the chromophores with larger chromophore concentrations. By introducing silver nanoparticles, it could be possible to enhance efficient the complexation ratio of the used complex in order to enhance also the light-induced phenomena of the material. This is one thing suggested for future studies.

The azobenzene molecule used in the experiments was DY7, a bisazobenzene molecule. The kinetics of DY7 is not well understood because of the second azo-bond. In order to efficiently study the effect of local field enhancement by plasmonic structures on the ligt-induced phenomena in azobenzene-containing polymer films, it would be important to use materials that are well-known.

The results give valuable information about the influence of metallic nanoparticles on the light-induced phenomena in azobenzene-containing polymer systems. If anyone is willing to make further studies on this specific subject, reading this thesis beforehand will save him/her a lot of trouble.

References

[1] J. Evans, *The history and practice of ancient astronomy*. Oxford University Press, 1998.

[2] I. Newton, *Opticks: or, A treatise of the reflections, refractions, inflections, and colours of light*. Printed for W. and J. Innys, 1718.

[3] Y. Zhao and T. Ikeda, *Smart light-responsive materials: azobenzene-containing polymers and liquid crystals*. Wiley-Interscience, 2009.

[4] I. Freestone, M. Meeks, Nigel ans Sax, and C. Higgitt, "The Lycurgus cup - a Roman nanotechnology," *Gold Bulletin*, vol. 40, no. 4, pp. 270–277, 2007.

[5] N. L. Mata, R. A. Radu, R. S. Clemmons, and G. H. Travis, "Isomerization and oxidation of vitamin a in cone-dominant retinas: a novel pathway for visual-pigment regeneration in daylight," *Neuron*, vol. 36, no. 1, pp. 69–80, 2002.

[6] T. Todorov, L. Nikolova, and N. Tomova, "Polarization holography. 1: A new high-efficiency organic material with reversible photoinduced birefringence," *Applied optics*, vol. 23, no. 23, pp. 4309–4312, 1984.

[7] C. Barrett, A. Natansohn, and P. Rochon, "Cis-trans thermal isomerization rates of bound and doped azobenzenes in a series of polymers," *Chemistry of Materials*, vol. 7, no. 5, pp. 899–903, 1995.

[8] M. L. Brongersma and P. G. Kik, *Surface plasmon nanophotonics*, vol. 131. Springer Berlin, 2007.

[9] F. Krollpfeiffer, C. Mühlhausen, and G. Wolf, "Zur kenntnis der lichtempfindlichkeit von aryl-β-naphtylamin-azofarbstoffen," *Justus Liebigs Annalen der Chemie*, vol. 508, no. 1, pp. 39–51, 1934.

[10] P. Rochon, E. Batalla, and A. Natansohn, "Optically induced surface gratings on azoaromatic polymer films," *Applied Physics Letters*, vol. 66, no. 2, pp. 136–138, 1995.

[11] A. Natansohn and P. Rochon, "Photoinduced motions in azo-containing polymers," *Chemical reviews*, vol. 102, no. 11, pp. 4139–4176, 2002.

[12] A. Priimägi *et al.*, "Polymer-azobenzene complexes: from supramolecular concepts to efficient photoresponsive polymers," 2009.

[13] A. Cembran, F. Bernardi, M. Garavelli, L. Gagliardi, and G. Orlandi, "On the mechanism of the cis-trans isomerization in the lowest electronic states of azobenzene: S0, s1, and t1," *Journal of the American Chemical Society*, vol. 126, no. 10, pp. 3234–3243, 2004.

[14] R. Hagen and T. Bieringer, "Photoaddressable polymers for optical data storage," *Advanced Materials*, vol. 13, no. 23, pp. 1805–1810, 2001.

[15] A. Priimagi and A. Shevchenko, "Azopolymer-based micro-and nanopatterning for photonic applications," *Journal of Polymer Science Part B: Polymer Physics*, 2013.

[16] C. J. Barrett, P. L. Rochon, and A. L. Natansohn, "Model of laser-driven mass transport in thin films of dye-functionalized polymers," *The Journal of chemical physics*, vol. 109, p. 1505, 1998.

[17] K. Sumaru, T. Yamanaka, T. Fukuda, and H. Matsuda, "Photoinduced surface relief gratings on azopolymer films: Analysis by a fluid mechanics model," *Applied physics letters*, vol. 75, no. 13, pp. 1878–1880, 1999.

[18] P. Lefin, C. Fiorini, and J.-M. Nunzi, "Anisotropy of the photo-induced translation diffusion of azobenzene dyes in polymer matrices," *Pure and Applied Optics: Journal of the European Optical Society Part A*, vol. 7, no. 1, p. 71, 1998.

[19] J. Kumar, L. Li, X. L. Jiang, D.-Y. Kim, T. S. Lee, and S. Tripathy, "Gradient force: The mechanism for surface relief grating formation in azobenzene functionalized polymers," *Applied physics letters*, vol. 72, no. 17, pp. 2096–2098, 1998.

[20] T. G. Pedersen, P. M. Johansen, N. C. R. Holme, P. Ramanujam, and S. Hvilsted, "Mean-field theory of photoinduced formation of surface reliefs in side-chain azobenzene polymers," *Physical review letters*, vol. 80, no. 1, p. 89, 1998.

[21] M. Saphiannikova and D. Neher, "Thermodynamic theory of light-induced material transport in amorphous azobenzene polymer films," *The Journal of Physical Chemistry B*, vol. 109, no. 41, pp. 19428–19436, 2005.

[22] M. L. Juan, J. Plain, R. Bachelot, P. Royer, S. K. Gray, and G. P. Wiederrecht, "Multiscale model for photoinduced molecular motion in azo polymers," *ACS nano*, vol. 3, no. 6, pp. 1573–1579, 2009.

[23] A. Ambrosio, P. Maddalena, and L. Marrucci, "Molecular model for light-driven spiral mass transport in azopolymer films," *Physical Review Letters*, vol. 110, no. 14, p. 146102, 2013.

[24] W. L. Barnes, A. Dereux, and T. W. Ebbesen, "Surface plasmon subwavelength optics," *Nature*, vol. 424, no. 6950, pp. 824–830, 2003.

[25] S. K. Ghosh and T. Pal, "Interparticle coupling effect on the surface plasmon resonance of gold nanoparticles: from theory to applications," *Chemical Reviews*, vol. 107, no. 11, pp. 4797–4862, 2007.

[26] F. Zhang, P. Chen, X. Li, J. Liu, L. Lin, and Z. Fan, "Further localization of optical field for flower-like silver particles under laser radiation," *Laser Physics Letters*, vol. 10, no. 4, p. 045901, 2013.

[27] L. N. Ng, *Manipulation of particles on optical waveguides*. PhD thesis, University of Southampton, Faculty of Engineering and Applied Science, 2000.

[28] C. Mätzler, "Matlab functions for mie scattering and absorption, version 2," *IAP Res. Rep*, vol. 8, 2002.

[29] C. Bohren and D. Huffman, "Light scattering and absorption by small particles," 1983.

[30] Q. Fu and W. Sun, "Mie theory for light scattering by a spherical particle in an absorbing medium," *Applied Optics*, vol. 40, no. 9, pp. 1354–1361, 2001.

[31] A. O. Govorov, W. Zhang, T. Skeini, H. Richardson, J. Lee, and N. A. Kotov, "Gold nanoparticle ensembles as heaters and actuators: melting and collective plasmon resonances," *Nanoscale Research Letters*, vol. 1, no. 1, pp. 84–90, 2006.

[32] A. G. Skirtach, C. Dejugnat, D. Braun, A. S. Susha, A. L. Rogach, W. J. Parak, H. Möhwald, and G. B. Sukhorukov, "The role of metal nanoparticles in remote release of encapsulated materials," *Nano letters*, vol. 5, no. 7, pp. 1371–1377, 2005.

[33] S. Xu, J. Shan, W. Shi, L. Liu, and L. Xu, "Modifying photoisomerization efficiency by metallic nanostructures," *Optics Express*, vol. 19, no. 13, pp. 12336–12341, 2011.

[34] J. H. Yoon and S. Yoon, "Photoisomerization of azobenzene derivatives confined in gold nanoparticle aggregates," *Physical Chemistry Chemical Physics*, vol. 13, no. 28, pp. 12900–12905, 2011.

[35] S. Wu, J. Shen, J. Huang, Y. Wu, Z. Zhang, Y. Hu, W. Wu, W. Huang, K. Wang, and Q. Zhang, "Ag nanoparticle/azopolymer nanocomposites: In situ synthesis, microstructure, rewritable optically induced birefringence and optical recording," *Polymer*, vol. 51, no. 6, pp. 1395–1403, 2010.

[36] J. Zhou, J. Yang, Y. Sun, D. Zhang, J. Shen, Q. Zhang, and K. Wang, "Effect of silver nanoparticles on photo-induced reorientation of azo groups in polymer films," *Thin Solid Films*, vol. 515, no. 18, pp. 7242–7246, 2007.

[37] J. Shen, S. Wu, J. Huang, Q. Zhang, and K. Wang, "Localized surface plasmon resonance effect on photo-induced alignment of films composed of silver nanoparticles and azopolymers with cyano or methyl substitutes on azobenzene moieties," *Thin Solid Films*, vol. 518, no. 8, pp. 2128–2133, 2010.

[38] D. Nazarova, L. Nedelchev, V. Dragostinova, and N. Berberova, "Influence of the size of nanoparticles doped in series of azopolymers on the photoinduced birefringence," in *Seventeenth International School on Quantum Electronics: Laser Physics and Applications*, pp. 877009–877009, International Society for Optics and Photonics, 2013.

[39] A. Franco, J. García-Macedo, G. Brusatin, and M. Guglielmi, "Aggregation of dipolar molecules in SiO2 hybrid organic–inorganic films: use of silver nanoparticles as inhibitors of molecular aggregation," *Journal of Nanoparticle Research*, vol. 15, no. 4, pp. 1–13, 2013.

[40] L. M. Goldenberg, O. V. Sakhno, T. N. Smirnova, P. Helliwell, V. Chechik, and J. Stumpe, "Holographic composites with gold nanoparticles: nanoparticles promote polymer segregation," *Chemistry of Materials*, vol. 20, no. 14, pp. 4619–4627, 2008.

[41] R. J. Moerland, J. E. Koskela, A. Kravchenko, M. Simberg, S. van der Vegte, M. Kaivola, A. Priimagi, and R. H. A. Ras, "Large-area arrays of three-dimensional plasmonic subwavelength-sized structures from azopolymer surface-relief gratings," *Mater. Horiz.*, vol. 1, pp. 74–80, 2014.

[42] P. Ahonen, D. J. Schiffrin, J. Paprotny, and K. Kontturi, "Optical switching of coupled plasmons of ag-nanoparticles by photoisomerisation of an azobenzene ligand," *Physical Chemistry Chemical Physics*, vol. 9, no. 5, pp. 651–658, 2007.

[43] M. S. Bradley and J. H. Krech, "High-pressure raman spectra of the acetone carbon-carbon stretch in binary liquid mixtures with methanol," *The Journal of Physical Chemistry*, vol. 96, no. 1, pp. 75–79, 1992.

[44] C. Henry, R. Logan, and K. Bertness, "Spectral dependence of the change in refractive index due to carrier injection in GaAs lasers," *Journal of Applied Physics*, vol. 52, no. 7, pp. 4457–4461, 1981.

[45] Sigma-Aldrich, "V3204 ALDRICH, 4-vinylpyridine," 2014. Online; accessed 22 January 2014,
URL: `http://www.sigmaaldrich.com/catalog/product/aldrich/v3204`.

[46] A. D. Rakic, A. B. Djurišic, J. M. Elazar, and M. L. Majewski, "Optical properties of metallic films for vertical-cavity optoelectronic devices," *Applied optics*, vol. 37, no. 22, pp. 5271–5283, 1998.

[47] J. Vapaavuori, A. Priimagi, and M. Kaivola, "Photoinduced surface-relief gratings in films of supramolecular polymer–bisazobenzene complexes," *Journal of Materials Chemistry*, vol. 20, no. 25, pp. 5260–5264, 2010.

[48] M. Virkki, M. Kauranen, and A. Priimagi, "Different chromophore concentration dependence of photoinduced birefringence and second-order susceptibility in all-optical poling," *Applied Physics Letters*, vol. 99, no. 18, pp. 183309–183309, 2011.

[49] V. Pale, T. Nikkonen, J. Vapaavuori, M. Kostiainen, J. Kavakka, J. Selin, I. Tittonen, and J. Helaja, "Biomimetic zinc chlorin–poly (4-vinylpyridine) assemblies: doping level dependent emission–absorption regimes," *Journal of Materials Chemistry C*, vol. 1, no. 11, pp. 2166–2173, 2013.

[50] D. Brown, A. Natansohn, and P. Rochon, "Azo polymers for reversible optical storage. 5. orientation and dipolar interactions of azobenzene side groups in copolymers and blends containing methyl methacrylate structural units," *Macromolecules*, vol. 28, no. 18, pp. 6116–6123, 1995.

[51] C. Barrett, A. Natansohn, and P. Rochon, "Thermal cis-trans isomerization rates of azobenzenes bound in the side chain of some copolymers and blends," *Macromolecules*, vol. 27, no. 17, pp. 4781–4786, 1994.

A Specification Sheets

30 nm PVP Silver Powder

Lot Number: DAG1179-DAG1386F

Diameter (TEM):	28.7 nm	**TEM - calculated BET:**	19.67 m^2/g
First Standard Deviation:	2.1 nm	**Particle Surface:**	PVP
Coefficient of Variation:	7.4 %	**Particle Form:**	Powder

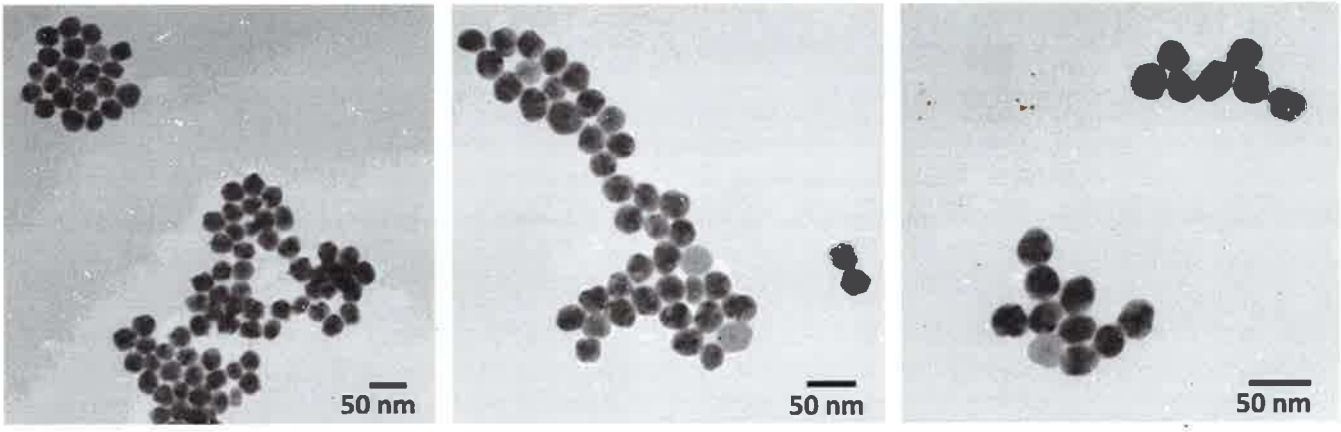

Size Distribution

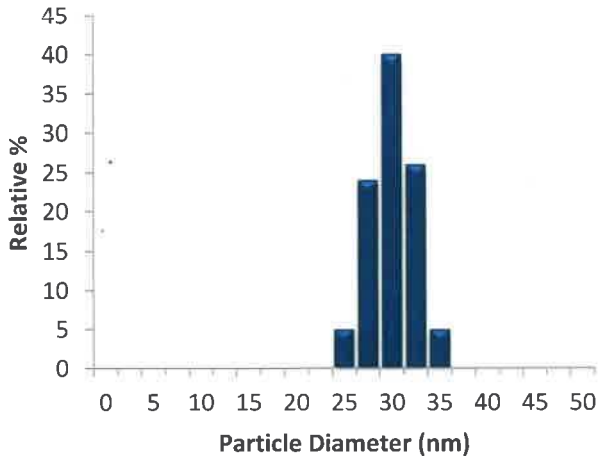

Optical Properties

When redispersed in water at 1 mg/mL

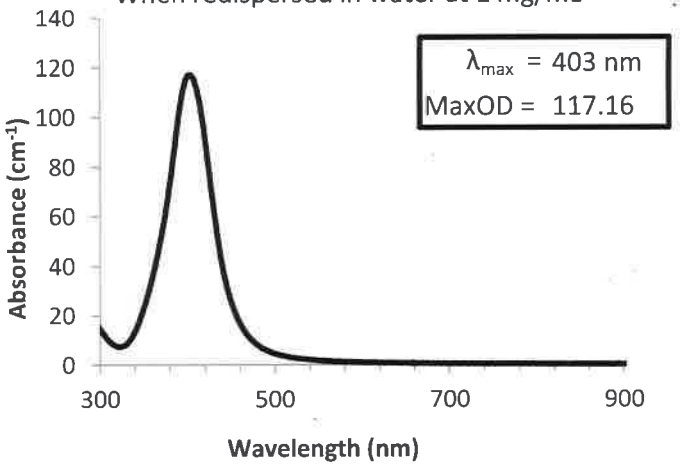

Characterization Instrumentation

Diameter and Size Statistics:	JEOL 1010 Transmission Electron Microscope
Mass Concentration:	Thermo Fisher X Series 2 ICP-MS
Spectral Properties:	Agilent 8453 UV-Visible Spectrometer
Hydrodynamic Diameter/Zeta Potential:	Malvern Zetasizer Nano ZS.

Storage and Handling: Cool, dry place away from light.
DO NOT FREEZE. AVOID INHALATION. Sonicate to resuspend.

nanoComposix, Inc
4878 Ronson Ct. Suite K
San Diego, CA 92111

For more information visit: www.nanocomposix.com

support@nanocomposix.com
Phone: (858) 565-4227
Fax: (619) 330-2556

50 nm PVP Silver Powder

Lot Number: JMW1007-DAG1386G

Diameter (TEM):	48.3 nm	**TEM - calculated BET:**	11.70 m^2/g
First Standard Deviation:	3.7 nm	**Particle Surface:**	PVP
Coefficient of Variation:	7.7 %	**Particle Form:**	Powder

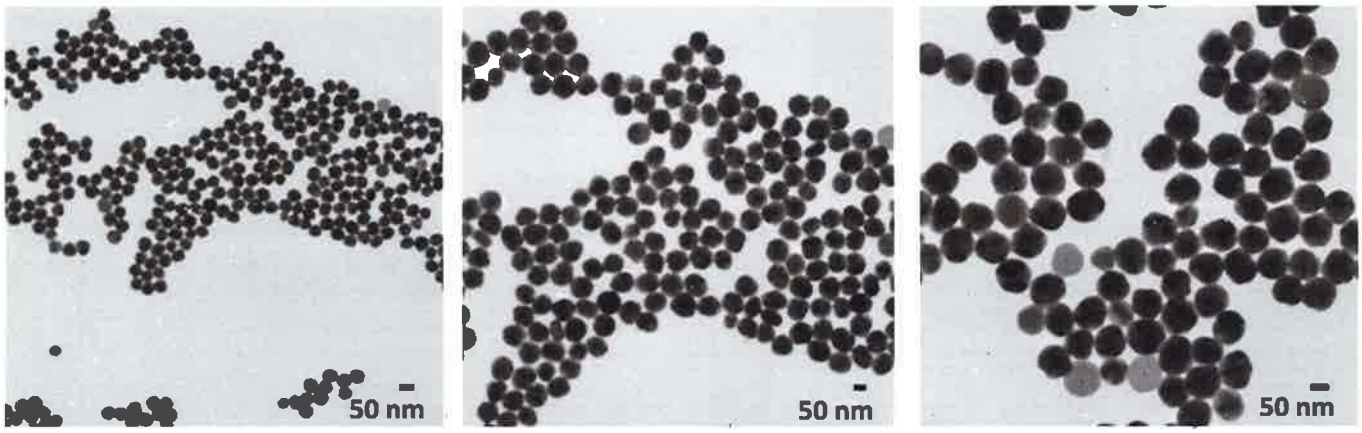

Size Distribution

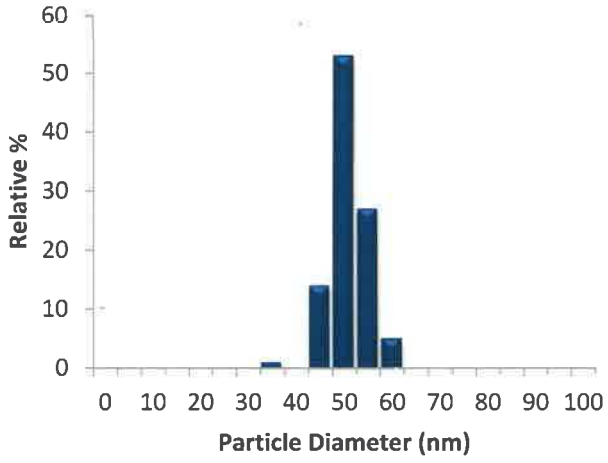

Optical Properties

When redispersed in water at 1 mg/mL

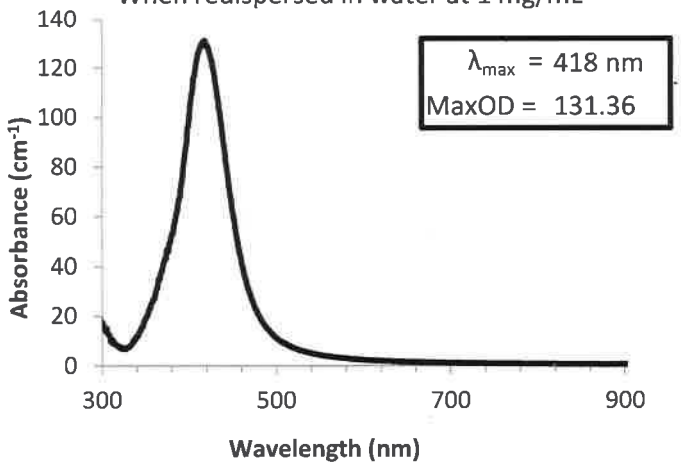

Characterization Instrumentation

Diameter and Size Statistics:	JEOL 1010 Transmission Electron Microscope
Mass Concentration:	Thermo Fisher X Series 2 ICP-MS
Spectral Properties:	Agilent 8453 UV-Visible Spectrometer
Hydrodynamic Diameter/Zeta Potential:	Malvern Zetasizer Nano ZS.

Storage and Handling: Cool, dry place away from light.
DO NOT FREEZE. AVOID INHALATION. Sonicate to resuspend.

nanoComposix, Inc
4878 Ronson Ct. Suite K
San Diego, CA 92111

For more information visit: www.nanocomposix.com

support@nanocomposix.com
Phone: (858) 565-4227
Fax: (619) 330-2556